Remote Sensing of Environment 237 (2020) 111544

Contents lists available at ScienceDirect

Remote Sensing of Environment

journal homepage: www.elsevier.com/locate/rse

Surface materials and landforms as controls on InSAR permanent and transient responses to precipitation events in a hyperarid desert, Chile

Teresa E. Jordan[a], Rowena B. Lohman[a,*], Lorenzo Tapia[b], Marco Pfeiffer[c], Chelsea P. Scott[d], Ronald Amundson[e], Linda Godfrey[f], Rodrigo Riquelme[b]

[a] Department of Earth and Atmospheric Sciences, Cornell University, Ithaca, NY, USA
[b] Departamento de Ciencias Geológicas, Universidad Católica del Norte, Antofagasta, Chile
[c] Departamento de Ingeniería y Suelos, Universidad de Chile, La Pintana, Santiago, Chile
[d] School of Earth and Space Exploration, Arizona State University, Tempe, AZ, USA
[e] Department of Environmental Science, Policy & Management, University of California at Berkeley, Berkeley, CA, USA
[f] Department of Earth and Planetary Sciences, Rutgers University, Piscataway, NJ, USA

ARTICLE INFO

Edited by Jing M. Chen

Keywords:
Sentinel
Soil moisture
Remote sensing
Soils
Active radar
Interferometric coherence

ABSTRACT

Ground-based monitoring and remote sensing of extreme rain events in the hyperarid Atacama Desert, Chile, reveal a complex relationship between precipitation, soil types and interferometric synthetic aperture radar (InSAR) coherence. These integrated analyses allow examination of temporal and spatial variations of the soil moisture response between locations dominated by sulfate soils and those with immature, silicate-mineral soils. The radar dataset captures at least four separate rain events within the 2015–2017 timeframe, two of which were regionally devastating. The lack of vegetation in this region allows us to discriminate between contributions to the InSAR coherence from permanent changes of the landscape (e.g., erosion or deposition) and transient changes associated with soil moisture variability. The spatial distribution and character of the transient InSAR response depends strongly on soil type, and is remarkably repeatable between rain events. The areas that experienced permanent changes included river channels, steep slopes, playas, and sites of anthropogenic activity, such as roads, mines, or telescope construction. Ground-based observations of soil moisture after each event also exhibit a strong dependence on soil type. The observations presented here demonstrate how InSAR data can constrain variations in soil moisture with high spatial resolution over large regions, complementing the higher-sensitivity but sparser field sites and enabling discrimination of inter-event variability and analysis of longer-term changes in soil mineralogy in arid regions.

1. Introduction

Constraints on soil moisture are valuable inputs for agricultural and water resource management (e.g., Dobriyal et al., 2012), weather forecasting, and climate dynamics research (e.g., Delworth and Manaba, 1993; Jung et al., 2010; Stocker et al., 2013, 2019). Soil moisture variability plays a role in the susceptibility of surfaces to erosion, through controls on infiltration rates and on the formation of salts and other minerals that increase the degree of induration of the soils (e.g., Davis et al., 2010; Owen et al., 2011). Satellite-based synthetic aperture radar (SAR) observations now provide near-global, regular coverage even at night or in the presence of clouds, resulting in proxies for soil moisture that can complement those from other sensors and ground observations and that capture the evolution of surface properties over time following a precipitation event. Variations in soil moisture impact both the amplitude and phase of radar imagery (e.g., Ulaby et al., 1979; Dobson and Ulaby, 1986; Nolan et al., 2003; Zwieback et al., 2013, 2017), and can be observed with both active and passive radar at a range of wavelengths (e.g., De Zan et al., 2014; Zribi et al., 2014). Coherence between SAR acquisitions can be affected by temporal changes in vegetation, sediment transport or other types of surface change that impact the location, orientation or composition of the individual scatterers within a given pixel (e.g., Zebker and Villasenor, 1992), as well as by variations in soil moisture. In this paper, we examine the temporal variations in coherence after rain events in a region with a hyperarid climate, including an assessment of the impact of soil type on the observed InSAR behavior across the study area and a comparison with in situ observations of soil moisture.

* Corresponding author.
E-mail addresses: tej1@cornell.edu (T.E. Jordan), rbl62@cornell.edu (R.B. Lohman), ltapiaesca@gmail.com (L. Tapia), mpfeiffer@uchile.cl (M. Pfeiffer), cpscott1@asu.edu (C.P. Scott), earthy@nature.berkeley.edu (R. Amundson), lvgodfre@eps.rutgers.edu (L. Godfrey), rriguelme@ucn.cl (R. Riquelme).

https://doi.org/10.1016/j.rse.2019.111544
Received 21 August 2019; Received in revised form 24 October 2019; Accepted 14 November 2019
Available online 24 November 2019
0034-4257/

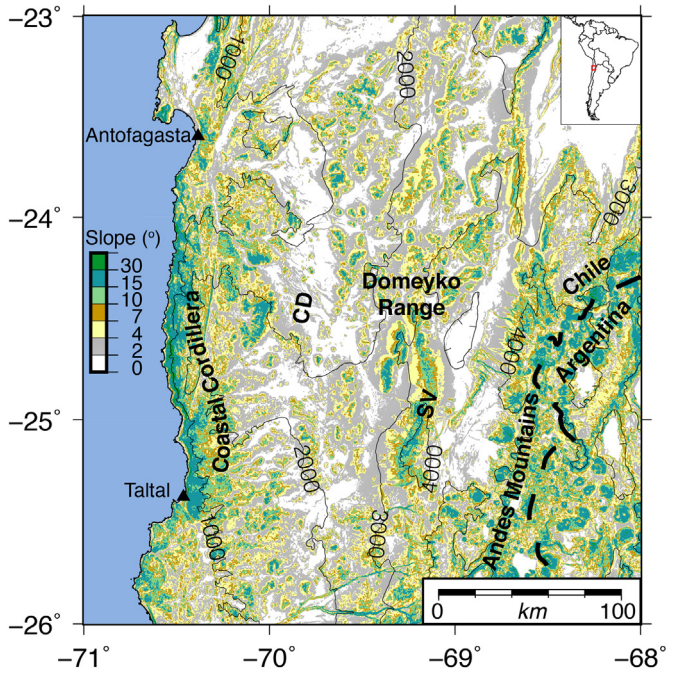

Fig. 1. Location and major features of landforms within study area: Slope of land surface (color, SRTM DEM, Farr et al., 2007), 1000 m contours (thin black lines, closed depressions indicated with tics), international boundaries (heavy dashed lines), Central Depression (CD), Sierra de Varas (SV) and locations of the coastal cities of Antofagasta and Taltal (black triangles). Study area location within South America shown as red box in inset. (For interpretation of the references to color in this figure legend, the reader is referred to the web version of this article.)

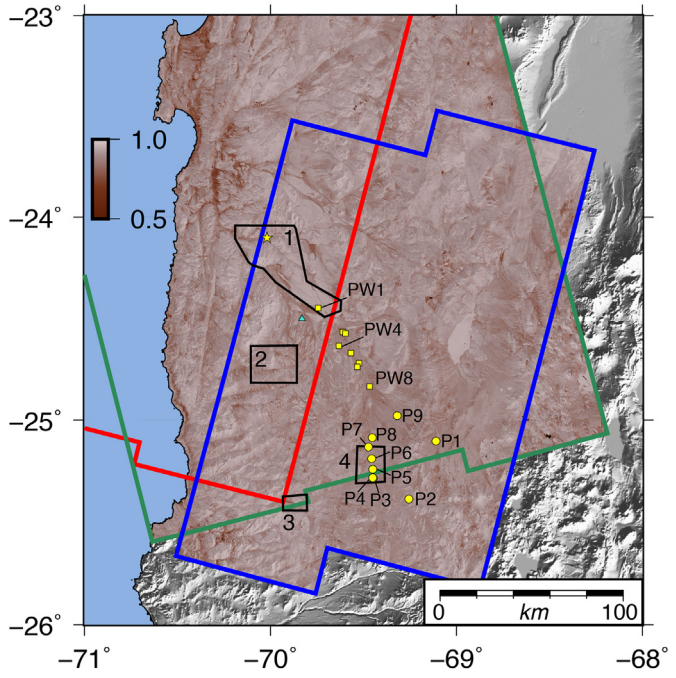

Fig. 2. SAR data coverage and field locations: InSAR background coherence (brown shading, described in Section 3) for the three tracks examined here, T54 (red), T156 (blue) and T47 (green), overlain on shaded topographic relief (Farr et al., 2007). Black outlined polygons numbered 1 to 4 indicate focus regions shown in Figs. 12–13. Yellow symbols indicate in situ instruments and field studies discussed in text, including the humidity sensor installation at Yungay (star), and soil pit observations (circles, P1–9, squares, PW1–8). Turquoise triangle indicates location of InSAR correlation timeseries shown in Figs. 5 and 6. (For interpretation of the references to color in this figure legend, the reader is referred to the web version of this article.)

We focus on the hyperarid Atacama Desert of Chile, 23°–26°S Latitude (Fig. 1) for the following three reasons. First, the almost complete lack of vegetation results in very high coherence between most pairs of SAR images, even spanning intervals of multiple years. This lack of vegetation allows us to separate out and better understand the effect of soil moisture changes in a manner that would not be possible in agricultural or heavily forested regions. Second, constraints on soil moisture in semi-arid to arid regions are critical inputs to numerical weather prediction and climate simulations (e.g., Mintz, 1982; Garratt, 1994; Chen and Dudhia, 2001; Koster et al., 2004), as well as for drought forecasting (e.g., Anderson et al., 2012; Hao et al., 2018) and modeling of flood severity (e.g., Sharif et al., 2017). Third, on a longer timescale, the understanding of how soils form and persist in arid to hyperarid regions, sometimes for millions of years, requires that we also understand the water budget and degree of erosion that occurs during the rare but extreme precipitation events that impact the area (e.g., Davis et al., 2010; Owen et al., 2011).

Over a three-year timespan, from 2015 to 2017, there were two extremely uncommon, major precipitation events in this area, as well as several smaller, more typical storms. Frequent (~12-day repeats) SAR image acquisitions from ESA's Sentinel 1A/B satellites (Table S1) allow characterization of surface change associated with erosion, deposition and variations in the water content within the shallow soil. The occurrence of repeated, widespread precipitation events covering an area of variable soil composition and almost no vegetation allows us to assess how well we can separate the impacts of permanent (i.e., erosion, deposition) and transient (i.e., soil moisture) contributions to the SAR coherence time series. Furthermore, the existence of ground-based observations of soil moisture in several locations (Fig. 2) offers an unusual opportunity to compare the in situ and remote sensing observations in a sparsely populated, hyperarid region.

In Section 2, we present a summary of the variations of surface properties within the region, including soil composition and vegetation. Sections 3 and 4 include descriptions of the InSAR processing and field observations of soil moisture and surface properties, respectively. In Section 5, we provide an overview of how SAR coherence varies within an approximately 63,000 km^2 study area in response to the precipitation events, then describe in detail the features of four characteristic sub-areas and their SAR responses. Section 6 includes discussion of the dependence of soil moisture response on soil type, including the observations that changes in sulfate mineralogy within the soils occurred without any permanent change in the SAR response at those locations.

2. Overview of the study area

2.1. Physiography

The study area includes major landform elements that extend from broad, nearly flat valley bottoms with dry lake beds, to high mountain peaks with little or no soil (Figs. 1, 3). The lower-relief portions of the landscape are dominated by gently inclined soil-mantled surfaces, on which soil compositions vary from mature soils whose dominant minerals are calcium sulfates to very immature silicate-mineral soils. From a geological perspective, the landscape has evolved very slowly; the geomorphological features which comprise gently inclined surfaces are of multiple origins and a wide range of antiquity (Amundson et al., 2012b).

The landscape in the study area rises from the Pacific Ocean on the west to about 1500 m above sea level (masl) across a narrow zone of steep terrain (Fig. 1, slope gradients > 30° west of Coastal Cordillera). East of that escarpment, for approximately 120 km inland, valley bottoms of the Central Depression range between 1000 and 2000 masl, summits of the Coastal Cordillera and the Domeyko Range are primarily

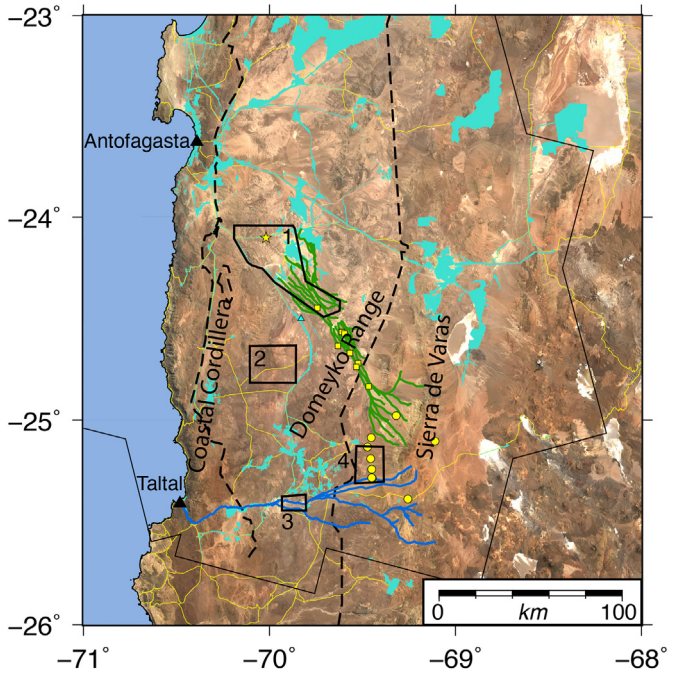

Fig. 3. Optical satellite images (Landsat) of the region of study. The road system (yellow lines), cities and regions shaded in turquoise have experienced extensive human disturbance of the land surface (Section S1). The two dashed black lines divide areas of calcium sulfate-dominated soils (between the two lines) from regions of silicate-mineral soils (near Pacific coast and east of the dashed line in center of image). Green and dark blue lines indicate the Quebrada El Profeta and Rio Chaco drainage systems, respectively. Other symbols are as in Fig. 2. Thin black line indicates region of InSAR coverage. (For interpretation of the references to color in this figure legend, the reader is referred to the web version of this article.)

below 3000 masl, and slopes are gentle (Fig. 1, gradients 0–7°). The Sierra de Varas in the eastern Cordillera Domeyko (Fig. 1, SV) and the Andes Mountains near the Chile-Argentina border rise above 4000 masl and are characterized by steep slopes (Fig. 1, eastern sector with slope gradients > 15°).

Constructional volcanic landforms within the study area are restricted to the Andes Mountains. Elsewhere, erosional landforms dominate, constructed on volcanic, plutonic, and Mesozoic-Cenozoic sedimentary rocks. Sedimentary landforms are common in the low gradient areas of the Central Depression and Domeyko Range, but these are almost entirely long-abandoned depositional landforms that were last active approximately 2 Ma (Amundson et al., 2012b). The only large areas of Quaternary deposition are closed drainage basins that form flat areas between the Domeyko Range and the Andes in the eastern part of the study area.

Although the drainage for most of the study area is endorheic, two major drainage catchments extend from the high eastern mountains to the Coastal Cordillera. The west-trending Chaco River (Fig. 3, blue), drains the southern region, from Sierra de Varas and the Andean volcanic peaks to the Pacific. The Quebrada El Profeta (Fig. 3, green), which drains much of the Sierra de Varas and northern Domeyko Range, terminates at the surface in a closed basin within the northern Central Depression, while its groundwater seeps through alluvium-filled valleys to the Pacific at the coastal city of Antofagasta (Herrera and Custodio, 2014).

2.2. Climate and vegetation

At low elevation (< 1000 m) near the coast, air masses from the Pacific deliver a small amount of rain (e.g., 11 mm per year in Taltal city) and fog-fed plants and sparse cacti occur. At intermediate elevations (~1000–3000 m; the Central Depression and all but the highest peaks of the Domeyko Range) occurs the hyperarid or "absolute" desert with < 5 mm/year of rain and almost no vascular plants (Díaz and Wright, 1965). The high elevation mountains of the eastern part of the study area receive > 20 mm/yr. of precipitation and support vegetation that includes bunch grass, perennials, annuals, and woody shrubs (Díaz and Wright, 1965).

Two significant, widespread precipitation events impacted the study region in recent years. From 24 to 26 March 2015, a warm-season storm brought rain and snow across the entire study area (Fig. 4a). The precipitation changed from rain to snow at about 3600 masl. Although an unprecedented 80–90 mm of liquid precipitation fell at some locations in both the mountains and the lowlands (Fig. 4a), within the very sparsely populated study area there was little property damage. A second significant precipitation event followed two years later, 6–7 June 2017, with widespread snowfall above 2700 masl and rain reported at many lowland gauges (up to 40 mm, Fig. 4d). A major difference between those two major precipitation events was the role of rain compared to snow: because runoff of surface water is delayed where snow accumulates, streamflow in response to the June 2017 event was delayed and diminished. Two smaller events between those dates were more typical of ordinary, albeit infrequent, Atacama Desert precipitation events. On 8–11 August 2015, a strong winter-season storm impacted the Pacific coastal region, dropping up to 30 mm of precipitation that caused infrastructure damage and deaths in cities built at the toe of the steep coastal mountain slope. Most interior stations received only trace amounts of rain (Fig. 4b). Another winter-season event, 25–27 June 2016, brought up to 22 mm rain to coastal communities and snow to the southeastern mountains. Only one interior rain gauge reported a few millimeters of precipitation (Fig. 4c).

2.3. Soils

Two major categories of soil occur in the study area. In regions where the climate is arid to only moderately hyperarid (western and eastern sectors of the study area), soils are very poorly developed. These immature soils are composed of little-weathered primary silicate minerals, small amounts of calcium carbonate, some gypsum cement, and less than a few percent clay (e.g., Díaz and Wright, 1965; Ewing et al., 2006). Where the climate is hyperarid, the soils are salty and sulfate-rich. Most of the salt is delivered by the atmosphere from a range of primary sources (e.g., sea salts, volcanic gases, weathered rocks), whose contributions vary across the study area (e.g., Ericksen, 1981; Rech et al., 2003; Michalski et al., 2004; Ewing et al., 2006; Cosentino et al., 2015). In addition to calcium sulfate, salts include relatively abundant sodium chloride and lesser amounts of highly soluble salts such as nitrates. Rain events infrequently wet the soil, dissolving some salts which then infiltrate downward. Later evaporation leads to formation of new minerals that more tightly cement the deep levels of the soil (Bao et al., 2004; Ericksen, 1981).

The dominant soil constituent, calcium sulfate, occurs as the minerals anhydrite ($CaSO_4$) and gypsum ($CaSO_4$-$2H_2O$). Across most arid regions on Earth, anhydrite rarely occurs under surface conditions as it is thermodynamically less stable than gypsum (Hardie, 1967). However, anhydrite occurs widely in the Atacama Desert. Rech et al. (2003), documented that "soil cements" at 20–30 cm depth were 0–40% anhydrite; Cosentino et al. (2015), determined that surface-collected Holocene soil farther north in the hyperarid region contains 0–100% anhydrite. Within the study area, Ewing et al. (2006), observed a vertical trend in calcium sulfate components of soils: anhydrite occurs with gypsum at the surface (0 to 3 cm), then only gypsum between depths of 3 and 40 cm, while mostly pure anhydrite occurs below 40 cm depth. While the conversion of anhydrite into gypsum occurs relatively quickly in the presence of water, the inverse process is not fully understood (Klimchouk, 1996). It has been reported that surface anhydrite may occur due to the dehydration of gypsum at temperatures above 42 °C

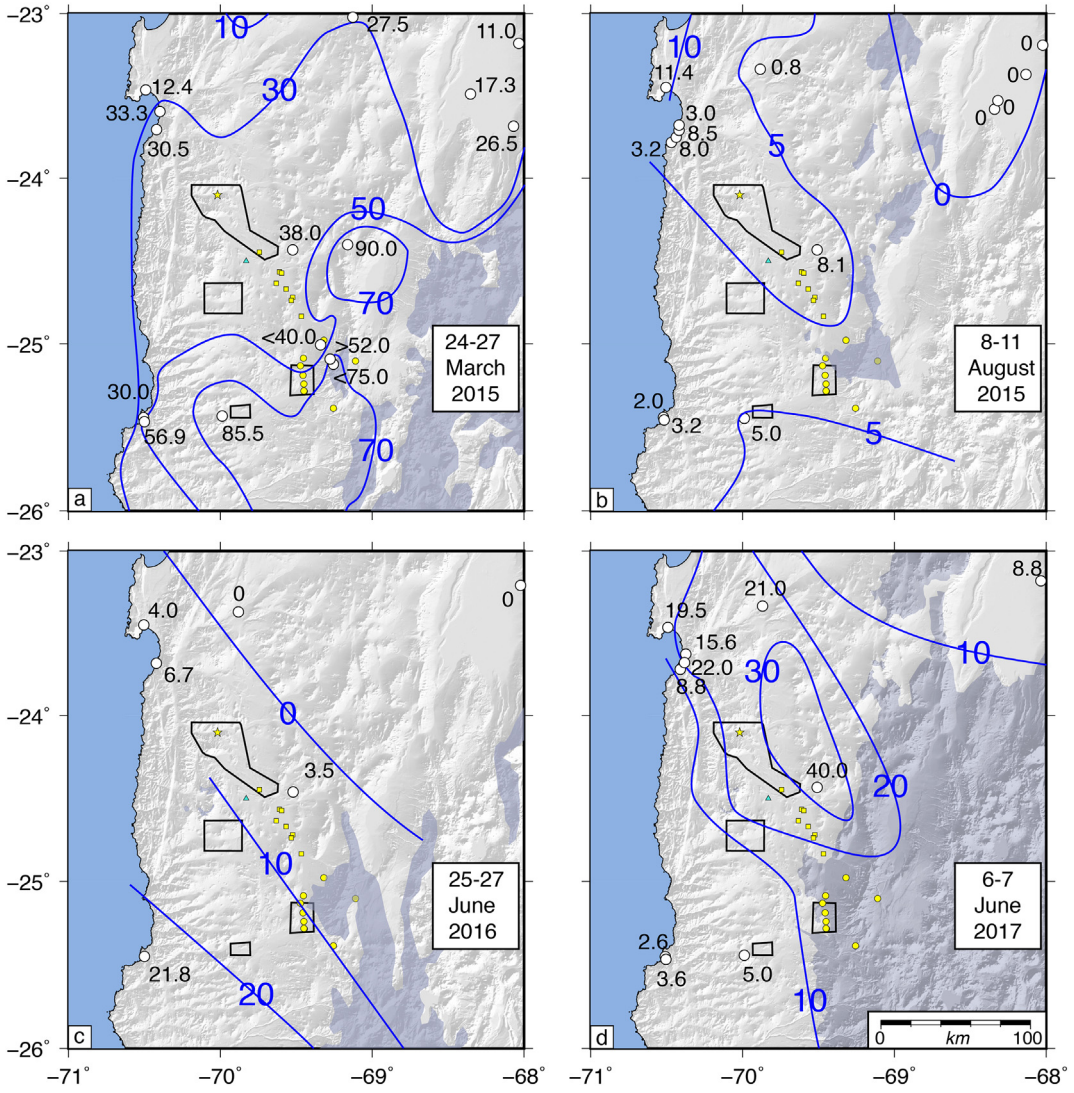

Fig. 4. Spatial distribution of precipitation: a) 24–27 March 2015. b) 8–11 August 2015. c) 25–27 June 2016. d) 6–7 June 2017. For each event, station data for liquid precipitation shown in millimeters, contours of total liquid rain (blue lines, labels in millimeters), and regions of snow accumulation (pale blue) are shown. (a), (b) and (d) are modified after Jordan et al. (2018); modifications and (c) are based on data from Dirección General de Aguas, Chile (Table S4). Other symbols as in Fig. 2. Fig. S8 shows additional stations covering a larger area. (For interpretation of the references to color in this figure legend, the reader is referred to the web version of this article.)

(James, 1992); this mechanism might explain its presence in the Atacama's shallowest soils. On the other hand, anhydrite can also directly precipitate from a high ionic strength solution (Freyer and Voigt, 2003), which might explain its presence at depths with high contents of halite in the Atacama Desert.

2.4. Anthropogenic impacts to surface

There has been very little anthropogenic disturbance over approximately 97% of the study area (Fig. 3). Active mining operations, inclusive of open pit and underground metals mining as well as surface lithium brine extraction and processing, today employ several thousand people within the study area. This is a region of extensive historical mining of nitrates from the unusual soils, particularly from the 1880's to 1960's (Espinoza et al., 2011). It is estimated that many more people were historically engaged in mining than today, and at various dates approximately 10,000 people once lived in three mining districts in the interior (Aguas Blancas, Taltal and Canton Central; Mercado, 2006; Espinoza et al., 2011). That historical activity disturbed wide tracts of land that have partially returned to a semi-natural condition. Categories of disturbed surfaces include modern highways and gravel roads, pipeline and power line corridors, historical cart tracks and railways, areas where mining has extracted or overturned the natural surface materials, and new installations of wind farms, solar farms and telescopes. Further details on our categorization of regions as anthropogenically disturbed can be found in the Supplemental Material.

3. InSAR observations and soil moisture

We use data acquired by the European Space Agency's Sentinel-1A/B satellites between October 2014 and February 2018, for three independent, overlapping tracks. We process the vertical-vertical (VV) polarization component of all potential interferometric pairs with data acquired between November 2014 and January 2018 using the InSAR Scientific Computing Software (ISCE) package (Rosen et al., 2012; Fattahi et al., 2017). We use between 29 and 65 dates for each of the three tracks (Fig. 2, Table S1), resulting in > 2000 combinations of dates for the tracks with the most data.

3.1. InSAR coherence

Interferometric coherence magnitude is a measure of the similarity in the reflective ground properties at the date of two SAR acquisitions. The complex-valued interferometric coherence between two SAR images is defined as (e.g., Born and Wolf, 1975; Zebker and Villasenor, 1992; Hanssen, 2001):

$$\gamma = \frac{<\nu_1 \nu_2^*>}{\sqrt{<\nu_1 \nu_1^*> <\nu_2 \nu_2^*>}} \quad (1)$$

where ν_i contains the complex-valued observation for each SAR image acquired at time i, ν_i^* is its complex conjugate, and $< \cdot >$ indicates the expected value. We estimate this expected value through a spatial average over a box with dimensions of fifteen pixels in range and four pixels in azimuth, corresponding to a ground dimension of approximately 88 m in range and 80 m in azimuth. The coherence magnitude, $|\gamma|$ approaches one where the radar scatterers have experienced little change in the position or characteristics and zero in regions where significant ground disturbance or other changes in surface processes has occurred between acquisitions (e.g., Zebker and Villasenor, 1992). In the rest of this paper we will refer to coherence magnitude as coherence, and will use γ instead of $|\gamma|$.

3.2. Soil moisture and coherence

The impact of soil moisture on interferometric phase and coherence (e.g., Ulaby et al., 1979; Nesti et al., 1995; Dobson and Ulaby, 1986; Nolan et al., 2003) has received renewed interest in recent years (e.g., Rabus et al., 2010; Zwieback et al., 2013; De Zan et al., 2014; Zwieback et al., 2014, 2015, 2017), in large part due to the increasing availability of dense time series of SAR imagery in many areas around the globe (e.g., European Space Agency, 2013). SAR in arid and hyperarid environments, in particular, has been explored as a means of deconvolving the soil, disturbance and vegetation effects, both in studies focusing on backscatter (e.g., Moran et al., 2000; Thoma et al., 2006; Mladenova et al., 2014; Hossain and Easson, 2016) and coherence at a range of wavelengths, including X-band (Baade and Schmullius, 2010) and C-band (e.g., Lee and Liu, 2001; Schepanski et al., 2012).

Variations in soil moisture change the strength of interaction between the radar signal and the scatterers distributed within the shallow subsurface. For the data examined here, the impact of individual precipitation events, as well as other factors, can be seen in the coherence timeseries at individual sites (Fig. 5) with characteristics that vary dramatically across the study area. We illustrate the coherence between all pairs of dates at a given point in space with an upper-triangular matrix where each row and column correspond to the dates of the available SAR data (Fig. 5a). The top row corresponds to all possible interferograms made with the first available date, and the diagonal corresponds to the set of "sequential" pairs, i.e., the shortest-time-span interferograms.

The observed coherence between any two dates at each location is dominated by three components: a background coherence that is determined by factors that include surface roughness and surface slope at that location, a permanent coherence loss within a given time interval (e.g., Zebker and Villasenor, 1992), and a transient term that likely involves a dependence on soil moisture:

$$\gamma_{ij} = \gamma^0 \gamma_{ij}^p \gamma_{ij}^s \quad (2)$$

where γ^0 is the "background" coherence due to surface roughness, slope, etc., γ_{ij}^p is the "permanent" coherence loss spanning the time interval between dates i and j, and γ_{ij}^s is the "transient" coherence loss that results from the difference in soil moisture between two dates. Transient coherence changes may also occur due to variations in vegetation, such as seasonal leaf-off/leaf-on fluctuations, but this is not a significant factor in this study area due to the lack of vegetation. "Permanent" coherence loss occurs within individual time intervals and accumulates with time, such that γ_{ij}^p for any interferometric pair is the product of the permanent coherence loss within all of the intervening time intervals:

$$\log(\gamma_{ij}^p) = \sum_{k=i}^{j-1} \log(\gamma_{k,k+1}^p) \quad (3)$$

We define s_i, a "soil moisture index" for each date, i, where we make the approximation that the transient term depends on the difference between two dates as:

$$log(\gamma_{ij}^s) = -abs(log(s_i) - log(s_j)) \quad (4)$$

Note the ambiguity in sign and overall shift for the full timeseries of s_i, in that we could arbitrarily shift the entire timeseries of s_i, by a constant or multiply by -1 without changing the predicted impact on coherence. We choose the convention that the dry values of s_i, are near unity, and that wet values are lower, approaching zero. Details on our method for inverting for these components are in Supplemental Section S2. Both a dry-dry pair and a wet-wet pair would be expected to have higher coherence than a pair between dates with differing soil moisture (e.g., De Zan et al., 2014). A key difference between the current work and our previous study in this region (Scott et al., 2017) is that here we allow permanent and transient changes to vary for each time interval, instead of fixing them to only occur during individual, fixed, rain events. This reduces the impact of signals from other time intervals

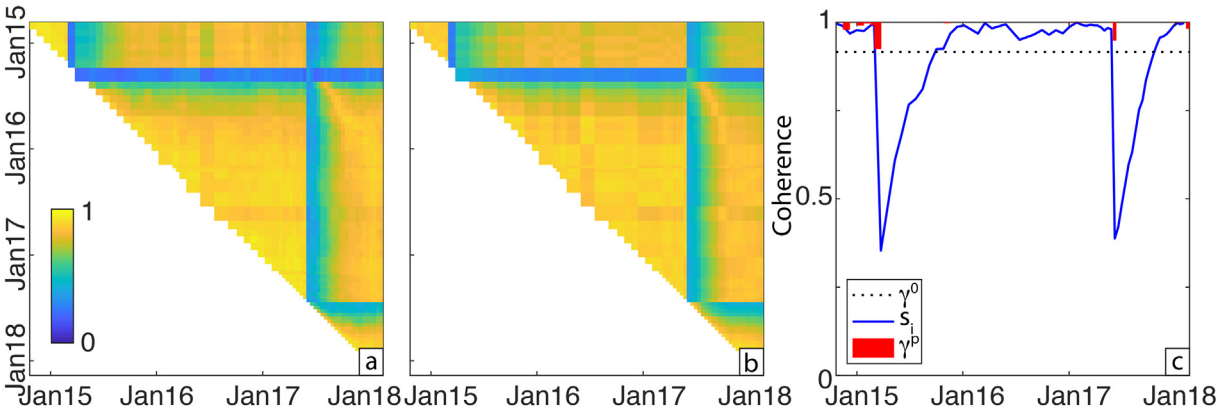

Fig. 5. Coherence data and model at a point. a) Coherence magnitude (see color scale) between all possible pairs of SAR images from Track 54, at location impacted by two storms (turquoise triangle, Fig. 2, latitude −24.502, longitude −69.830). b) Best fit to data in (a) using Eq. (2) with terms shown in (c). c) Surface roughness, soil moisture index, and permanent coherence loss terms (Eqs. (2)–(4)) inferred using the full set of coherence magnitude data (i.e., all pairs of SAR images) in (a). (For interpretation of the references to color in this figure legend, the reader is referred to the web version of this article.)

(e.g., anthropogenic activity) on each event.

To better characterize each precipitation event, we solve for the magnitude, $A_j(x)$, and characteristic timescale, $T_j^c(x)$, of the exponential decay that best fits the soil moisture index variations (s_i) following each of the $j = 4$ known rain events (Fig. 4) and at every location, x:

$$s_i(x) = \sum_{j=1}^{n} A_j(x) e^{(t_j - t_i)/T_j^c(x)} H(t_i - t_j) \quad (5)$$

where t_i and t_j refer to the time of the SAR image and the rain event, respectively, and H is the Heaviside function.

Permanent loss of coherence during a given time interval occurs when there are permanent changes to the radar scatterers within a pixel. This may be due to channelized flow of surface water that erodes in some locations or delivers sediment in others. Mineral transformations brought about by a rain event, such as the conversation of anhydrite ($CaSO_4$) to gypsum ($CaSO_4{\cdot}2H_2O$), or destabilization of the fragile, very porous structure of anhydrite-rich soil, hypothetically might also be accompanied by a permanent loss of InSAR coherence. We find that regions with anthropogenic disturbance, including mines and roads, are particularly prone to permanent coherence loss during rain events (e.g., regions indicated in turquoise in Fig. 3; Supplemental material).

3.3. Coherence changes associated with precipitation events within the study area

The major precipitation events of 2015–2017 were associated with localized permanent (Fig. 7, Fig. S1), and widespread transient coherence loss (Fig. 8). Rivers, low-lying areas like playas and closed basins, and areas with anthropogenic activity (see Supplemental material) had particularly strong permanent coherence losses (Fig. 7) when compared to surrounding areas. Where data from all three tracks are present, we observe very strong similarity in the coherence behavior (Fig. 6).

The largest events in March 2015 and June 2017 resulted in a transient coherence change over most of the study region (Fig. 8a, d) while the smaller events only impacted a portion of the region (Fig. 8b, c). Surfaces that responded to one event have a similar magnitude of response each time that it rains (Fig. 6), i.e., the sites that have more developed soil profiles show a strong response while adjacent regions with little to no soil often show no transient coherence change during the events.

In regions where snow fell (hatched regions with pink outline in Figs. 7 and 8), we avoid drawing any conclusions about the time series during these events. However, note that there are many regions that did experience snow that do not show permanent coherence loss (Fig. 7), indicating that the precipitation, melting and runoff did not impact the scatterers within those regions to any great extent. Note that, for the June 2016 event, the transient coherence change (Fig. 8c) is limited to a relatively narrow swath, but that the small-spatial-scale pattern of response in areas where it did rain is similar to what occurred during the large events. In Section 5, we focus on these quantities within the individual mapped regions 1–4.

The characteristic timescale, $T_j^c(x)$, from Eq. (5) also varies spatially over the study area as well as between events (Fig. 9). In areas where $A_j(x)$, is small, $T_j^c(x)$, is poorly constrained, so the best comparisons between precipitation events (Fig. 9c) are for the regions with significant transient coherence response. These areas also tend to be the lower-relief areas associated with alluvial fans and playas that are the focus of this paper. The region with the largest, most spatially extensive change in timescale (red, in Fig. 9c) is the inland area near 24° S latitude, covering much of Map area 1 and the Yungay site (red, in Fig. 9c). While the ground-based measurements of precipitation in that area are sparse in 2015 (Fig. 4), the shorter timescales shown in Fig. 9a relative to Fig. 9b in the northern portion of the Map area 1 is consistent with a smaller amount of rainfall in this area in March 2015, than in June 2017. The pattern of variability within the sector of shorter timescale (i.e., NNW-trending streaks) aligns with the prevailing winds during the 2015 event, which came from the NNW (Jordan et al., 2015, 2018).

4. Soil property materials and methods

4.1. Characterization of surface materials

Field observations of surface materials and landforms at specific points were conducted both before the March 2015 precipitation event, and in a series of field visits throughout the time span of the InSAR coherence analysis (Table S6). On each occasion, we marked locations of landforms with evidence of water-driven erosion or deposition in the recent past, described and photographed the forms, and described the properties and condition of surface materials. We also mapped the surface materials using geomorphological and optical attributes visible in satellite data available through Google Earth, in consultation with published geological maps, soil maps, and reports (Díaz and Wright, 1965; SERNAGEOMIN, 2003; Ewing et al., 2006, 2008; Espinoza et al., 2011; Ramos et al., 2015) as well as personal ground-based observations (Tables S7– S10).

The approximate east and west boundaries of the region of calcium sulfate soil and the areas of human impact were mapped over the entire 63,000 km^2 region (Fig. 3). In optical imagery, surfaces with calcium sulfate soils (Bao et al., 2004; Ewing et al., 2006; Rech et al., 2003; Owen et al., 2013) are generally characterized by a light gray tone, with patches of white (Fig. 3). We mapped the calcium sulfate soil boundaries, focusing on areas known from ground-based observation to be

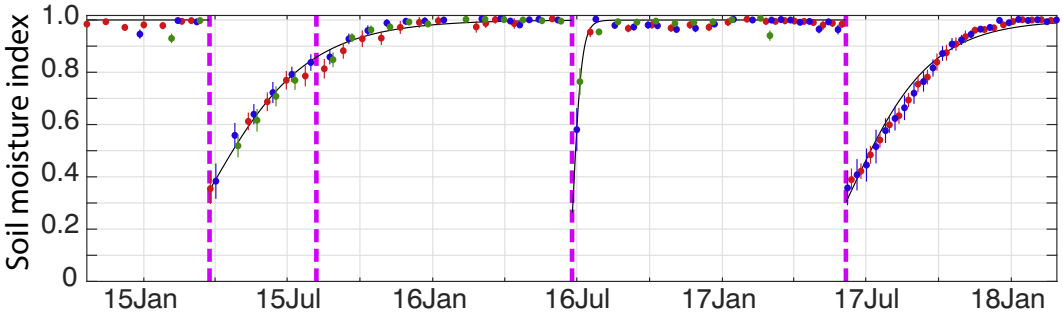

Fig. 6. Soil moisture index, s_i, observed by all three tracks: Same location as in Fig. 5, with s_i values (Eq. (4)) colored by T54 (red), T156 (blue) and T47 (green). Pink dashed lines indicate timing of rain events in this study (see Fig. 4). Black curve is best-fit exponential decay beginning at the time of each rain event (Eq. (5), map view of A_j for the individual rain events shown in Fig. 8). Error bounds show the standard deviation of a 5 × 5 pixel region around the target pixel. Note that the August 2015 event does not significantly impact the radar data at this location, although other regions of the study area are associated with significant coherence changes (Fig. 8b). (For interpretation of the references to color in this figure legend, the reader is referred to the web version of this article.)

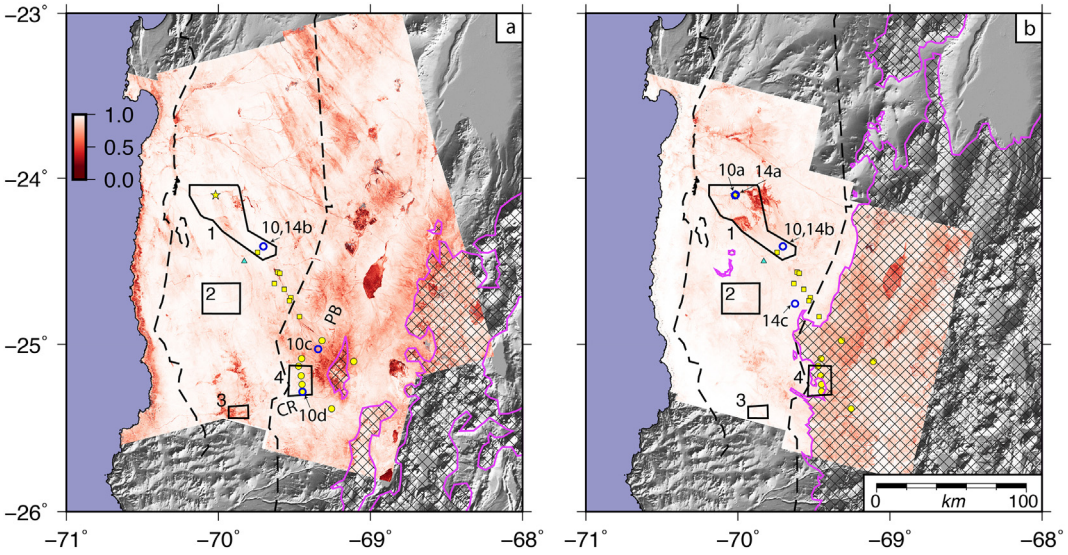

Fig. 7. Permanent coherence loss: γ^P, for the March 2015 (a) and June 2017 (b) events. Snow cover is shown by hatched region with pink outline. Other symbols as in Fig. 2. Results for other two rain events, which had far less impact, are in Fig. S1. Differing spatial coverage over time in this and following figures is a result of changes in the satellite data coverage over time. Blue circles indicate locations shown in Fig. 10 and Fig. 14. PB = Profeta Basin, CR = Chaco River. (For interpretation of the references to color in this figure legend, the reader is referred to the web version of this article.)

near a soil type transition. We estimate the local uncertainty on these simplified mapped boundaries (Fig. 3) to be ± 10 km.

Spatially comprehensive mapping of natural materials was conducted in four sub-areas that range in size from approximately 100 km^2 to 1200 km^2 (Fig. 2, Table S3). The areas were selected to focus on surface materials of several major geomorphological and geological categories, to examine regions with different InSAR coherence signatures, and to take advantage of ground-based soil moisture observations.

4.2. Ground-based soil moisture observations

Two methods were used to assess in situ soil moisture from the region. The first soil moisture dataset comes from physical samples along depth profiles sampled on dates shortly after the March 2015 rain event as well as up to two samples taken within the following year. The second dataset, for one location dominated by calcium sulfate soil, is a time series of the vertical profile of humidity in the soil pore spaces. These data span 4 to 19 months after the March 2015 rain event, and again from 0.5 to 4 months after the June 2017 precipitation event.

For the first dataset, soil moisture was obtained from physical samples in depth profiles at 16 sites near the center of the study area (Fig. 2: yellow squares and boxes). Most of these sites occur where 35–70 mm of rain fell 24–26 March 2015; that storm covered the easternmost site (Fig. 2, P1) with snow. At nine locations in the eastern area with silicate-mineral immature soils, pits 40–60 cm deep were dug 4–5 April 2015 (yellow circles, Fig. 2, within or near map area 4). Samples of the bulk soil excluding large rock fragments were collected at intervals of approximately 10 cm, stored in sealed plastic bags, and refrigerated until later laboratory analysis. At all pits, the particle sizes and compositions of soil materials, horizonation of the soils, and presence or absence of plant roots and debris were recorded. A second set of pits was dug 3–5 June 2015 at distances of 1.5 m to 2.0 m from the initial pits P4, P5, P7, to depths of 160–200 cm. Heavy snow fell between 25 and 27 May 2015 on higher elevation terrane only 20 km from these soil pits (Table S4), suggesting that rain may have fallen on the surface where profiles were sampled in early June. Over a year later, 16–17 June 2016, another pit was dug and sampled to 100 cm depth at location P4. Snow fell a few days earlier (11–14 June 2016) in the mountains nearby (Table S4), suggesting that rain may have fallen recently at P4. In the central sector of the study area, where calcium sulfate soil dominates, soil moisture data were collected once during the time period 20–23 July 2015, at eight soil pits (Fig. 2, yellow squares). Soil pits were dug to depths of 85–105 cm and approximately 300 g of soil was sampled at 15 cm depth intervals.

To determine the soil water content, approximately 100 g of soil comprised by particles smaller than a #4 mesh were weighed, dried in an oven maintained at 60 °C (± 5 °C) for 24 h, and weighed again in a laboratory, following a procedure specified by Chile's soil mechanics norm (Reyes et al., 1979) to determine the soil water content. Unquantified errors in the reported soil moisture content likely accumulate through the steps of exclusion of large rock fragments, storage, and handling during transfer into and out of the oven. In total, we estimate the reported soil moisture content (Table S5) to have uncertainties of about ± 2%.

The second method of soil moisture assessment was conducted at a location in the northwestern part of the SAR analysis region, Yungay (Fig. 2; star), within detailed map area 1. The humidity in pore spaces in a calcium sulfate soil was measured from August 2015 through October 2017, with a 6-month gap. Weather station data (Table S4) suggest that this location received about 30 mm of rain 24–26 March 2015, perhaps 5 mm of rain 8 August 2015, trace amounts 25 June and 8 July 2016, and 20–30 mm of rain 6 June 2017. Hoboware® soil humidity and temperature sensors were installed between 1 cm and 80 cm depths, most spaced at 10 cm intervals. The manufacturer reports that measurement uncertainty varies with the magnitude of relative humidity, such that for nearly all recorded dates the uncertainty in these data should be ± 2.5 to 3.5%. For the early weeks after the June 2017 rain event, the uncertainty was likely ± 5%.

Data were logged between 22 August 2015 and 17 November 2016 as well as between 25 June and 15 October 2017, captured at 30-minute intervals. For this paper, humidity values at depths of 10 cm, 30 cm, and 50 cm are examined, and simplified by using only humidity values recorded at a local time near 14:00 h each day, early in the afternoon. This eliminates diurnal variations which are a strong part of the signal at the shallowest depth. Soil humidity can be related to soil water potential by using the following thermodynamic expression for equilibrium conditions between the liquid and vapor phases for water in aqueous solutions (e.g., Van Genuchten, 1980):

$$\psi = RT/V_\omega \ln h \quad (6)$$

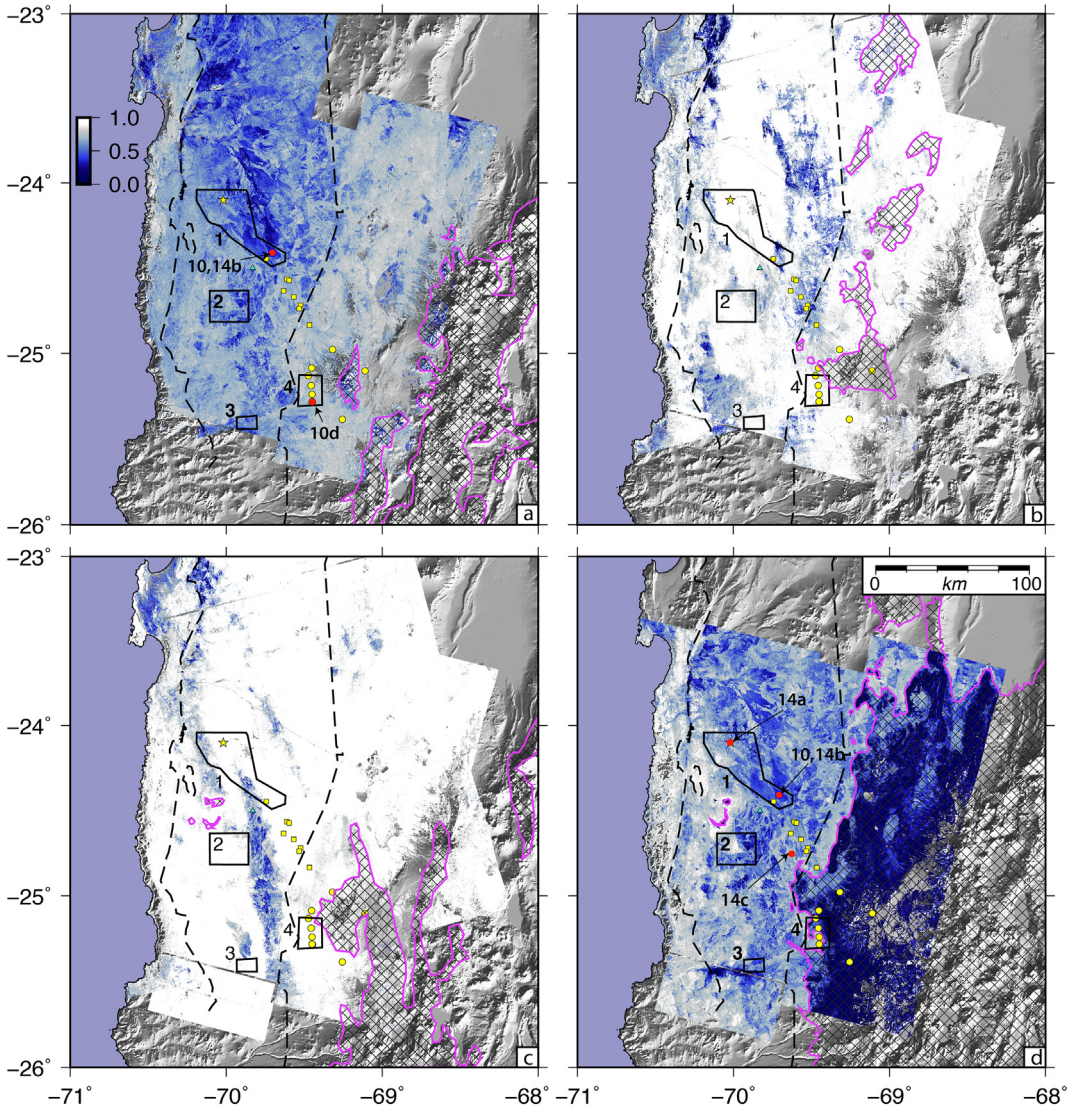

Fig. 8. Transient coherence loss: Magnitude of the best-fit exponential decay of s_i (e.g., Fig. 6, Eq. (5)), $A_j(x)$, following the March 2015 (a), August 2015 (b), June 2016 (c) and June 2017 (d) events (rain distribution shown in Fig. 4). Red circles indicate locations shown in Figs. 10 and 14, other symbols as in Fig. 7. (For interpretation of the references to color in this figure legend, the reader is referred to the web version of this article.)

where ψ is water potential (bars), T is temperature (K), V_ω is partial molal volume of water (1.8×10^{-5} m^3/mol at 4C), R corresponds to the universal gas constant (8.31×10^{-5} m^3 bar $mole^{-1}$ K^{-1}) and h is the fraction equilibrium relative humidity. We related the soil relative humidity to soil water content based on the best fit to a soil water characteristic curve of Van Genuchten (1980) obtained from water retention pairs from a soil core of 30 cm depth at Yungay.

5. Results

The predominance of $CaSO_4$-rich soils, which seem to control the magnitude and timescale of the transient InSAR coherence response, varies greatly from west to east. In a band 10–30 km wide near the coast (Fig. 3), the surficial layer is dominated by rock and by physically disaggregated rock fragments; there appears to be little calcium sulfate-rich soil. Principal rock compositions correspond to intermediate to mafic igneous lithologies, metasedimentary rocks, and sandstones (SERNAGEOMIN, 2003). Similarly, in the east, in the high-altitude sectors of the Domeyko Range and Andes Mountains, the surface materials are rock, physically disaggregated rock, and sedimentary deposits of these materials in alluvial and colluvial accumulations. There has been little chemical weathering of the silicate minerals, and, due to a lack of vegetation, there is little calcium carbonate in the soil. $CaSO_4$ is a minor component of the soil primarily where it is transported by the wind from western sources, funneled through the major cross-cutting valleys. Between those zones exists a 40–100 km wide region in which $CaSO_4$-rich soils cover much of the landscape (Fig. 3), over bedrock as well as over unconsolidated alluvial and colluvial sediments.

Observations of small scale landforms made during visits to the field after the precipitation events of March 2015 and June 2017 (Fig. 10) revealed that permanent changes to InSAR coherence often occurred in areas that experienced erosional loss (Fig. 10a, c) or depositional gain of sediment. In contrast, for locations with a strong transient InSAR coherence response in the months following these two events, the small scale topography after a major precipitation event was quite smooth and centimeter-scale vertical discontinuities were rounded, both of which are forms that suggest that the positions of the surface constituents had been stable for long periods of time (Fig. 10b, d).

5.1. Landforms associated with permanent InSAR coherence loss

Permanent coherence loss associated with the March 2015 extreme

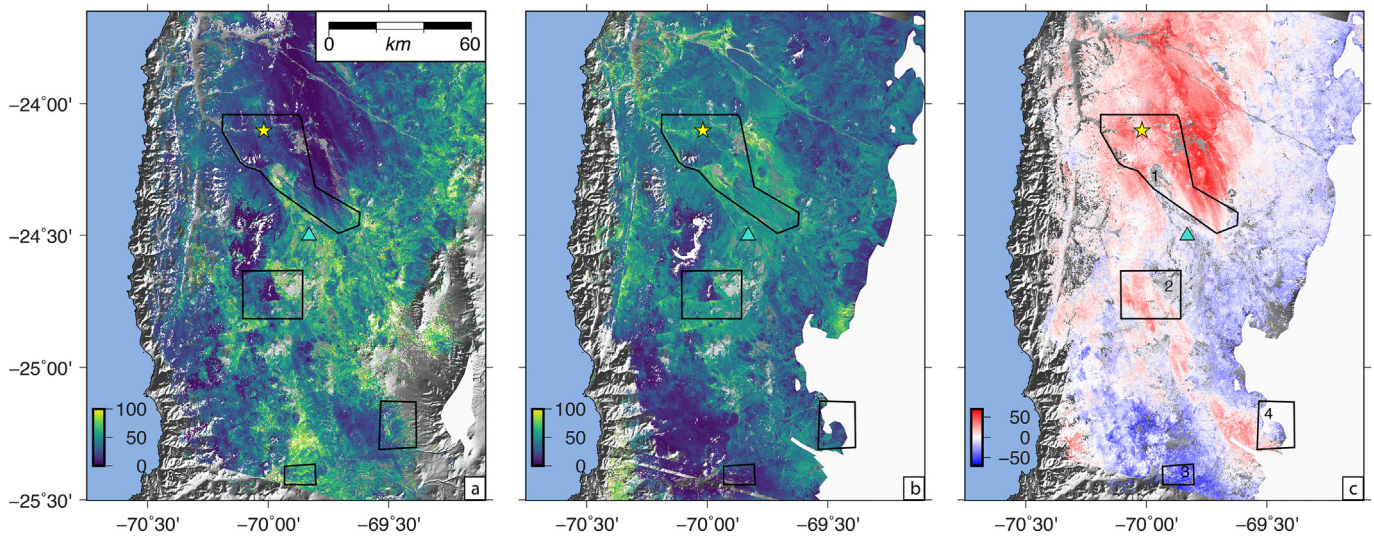

Fig. 9. Timescale variations: Characteristic timescale in days for the best-fit exponential decay of s_i (e.g., Fig. 6, Eq. (5)), $T_j^c(x)$, following the March 2015 (a) and June 2017 (b) events (rain distribution shown in Fig. 4). c) Difference in timescale, June 2017–March 2015. Red indicates longer timescale for the June 2017 event. Snow cover shown in white; other symbols as in previous figures. (For interpretation of the references to color in this figure legend, the reader is referred to the web version of this article.)

Fig. 10. Landforms that distinguish areas that suffered permanent InSAR coherence loss compared to transient InSAR coherence loss: a) In area of calcium-sulfate dominated soil, a minor ephemeral stream channel was activated by surface flow during the June 2017 precipitation event. Orange notebook is 19 cm in length. b) In area of calcium-sulfate dominated soil, a surface with no permanent InSAR change but a strong transient signal after both precipitation events. The irregular dark lines mark soil polygons. c) In area of silicate mineral soil, a broad ephemeral stream channel activated by surface flow during the March 2015 precipitation event. d). In area of silicate mineral soil, a relict alluvial surface with a weak transient InSAR signal following the March 2015 event. Photo locations shown in Fig. 7.

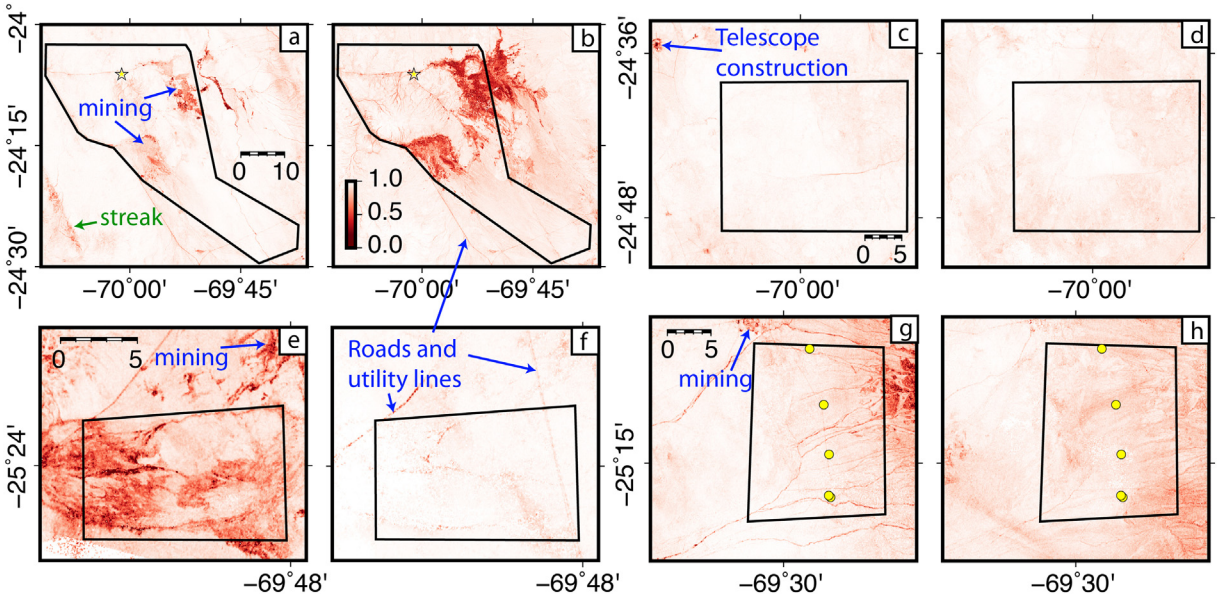

Fig. 11. Permanent coherence loss within mapped sub-regions: γ^p for the March 2015 (a, c, e, g) and June 2017 (b, d, f, h) events, for mapping area 1 (a, b), 2 (c, d), 3 (e, f) and 4 (g, h). Polygons and soil moisture measurement locations as in Fig. 2. Blue arrows and annotations indicate examples of anthropogenically disturbed zones. "Streak" in (a) is one of several bands of permanent coherence loss that align with prevailing wind directions (Fig. 7a). Distance scale in km. (For interpretation of the references to color in this figure legend, the reader is referred to the web version of this article.)

precipitation event was primarily focused on regions where the surface materials were easiest to mobilize, including areas of human disturbance and landforms where overland flow was focused during the event, especially ephemeral channels (Figs. 7, 11; S1). Permanent coherence loss associated with this event also exhibited NW-SE-trending streaks that cut across topography and across transitions in surface materials, which align with prevailing winds during the storm, up to 100 km in length (Fig. 7a, Scott et al., 2017). Field observations confirm that these streaks correspond to locations that experienced overland flow of liquid water and associated erosion, supporting the interpretation that the streaks were associated with heavy concentrations of rainfall (Figs. 7, 11a).

5.2. Transient InSAR responses to spatially variable landforms and surface materials

The magnitude and timescale of the transient InSAR coherence response associated with each event displays a complex spatial pattern (Figs. 8, 9, 12, 13). Within the central zone of $CaSO_4$-rich soil cover, both major precipitation events (Fig. 8a, d) produced a strong transient coherence response which lasted for > 6 months (Figs. 6, 12d), with a strong repeatability from event to event that can be seen in Figs. 12 and 13. Regions dominated by silicate soils, including much of Map area 4, had a much lower transient coherence response, although snow cover over much of the area in June 2017 limits our ability to constrain the evolution of coherence in that region. Sentinel data coverage improved greatly over time (Table S1), so the later events are better-constrained than the March 2015 event. The two weaker precipitation events are associated with narrower zones of transient InSAR coherence response, following the same dependence on surface soil type as the larger ones. In general, values of s_i in areas dominated by immature, silicate-mineral soils recover to their pre-rain conditions within several weeks or less, whereas areas with $CaSO_4$-rich soil recover much more slowly, over months or more (Figs. 6, 9).

The four mapped sub-regions, summarized in Table 1, encompass areas where the soil parent material is dominated by alluvial surface materials as well as areas dominated by exposed bedrock with thin soil and colluvium. Alluvial surfaces are dominated by soils of calcium sulfate composition in areas 1–3 (Fig. 14a, b) and by silicate mineral soils in area 4 (Fig. 14c).

Map area 1 displays some of the largest, and longest-lived, transient coherence responses observed in the study area (Fig. 12b, c, d), for both of the two major precipitation events. The strength of the response varies with the extent of coverage of thick $CaSO_4$ soil caps. The strongest transient responses are observed in the areas with the most developed calcium sulfate soils. In the southern sector, areas with eolian sand draped over the calcium sulfate soil also responded very strongly.

Map area 2 is dominated by a central region of Jurassic volcanic and sedimentary units (J3i of SERNAGEOMIN, 2003) that stand 200–300 m higher in elevation than surrounding areas, with slopes that exceed 10° and with only thin soils. These high peaks exhibit the lowest transient coherence loss in this region for each event (Fig. 13b, c). The surrounding, lower relief alluvial fans behave in a similar fashion as those in Map area 1.

In Map area 3, there is a clear distinction between the strong transient coherence change associated with calcium sulfate-soils and small change where there are fluvial channel sediments associated with the Chaco river (Fig. 13d, e). However, the large amount of permanent coherence change at this site (Fig. 11e) makes it more challenging to deconvolve the different factors contributing to coherence change (Eq. (2)). In general, older alluvial surfaces correspond to a somewhat stronger transient InSAR response than occurs where fluvial sediment is young.

Map area 4, which contains five of the soil moisture pits, is dominated by silicate-mineral soils. The area displayed little transient coherence response to the two major events (Fig. 13h, i). A strong coherence response occurred in only one small zone located within an area of calcium sulfate soil in the extreme southwest of the area, beyond the region of field mapping. Snowfall during the June 2017 event results in poor constraints on the coherence variations during that time period relative to those in 2015. Fig. S6 shows full time series of coherence at each of the individual soil pit sites.

5.3. Soil characteristics and soil moisture variability

The Yungay soil humidity site (Fig. 3, yellow star) and soil pits PW1-PW7 occur in the central zone of $CaSO_4$-rich soil. Below a gravel layer about 3 cm thick, the Yungay site and four pits (Table S5, PW1, PW2,

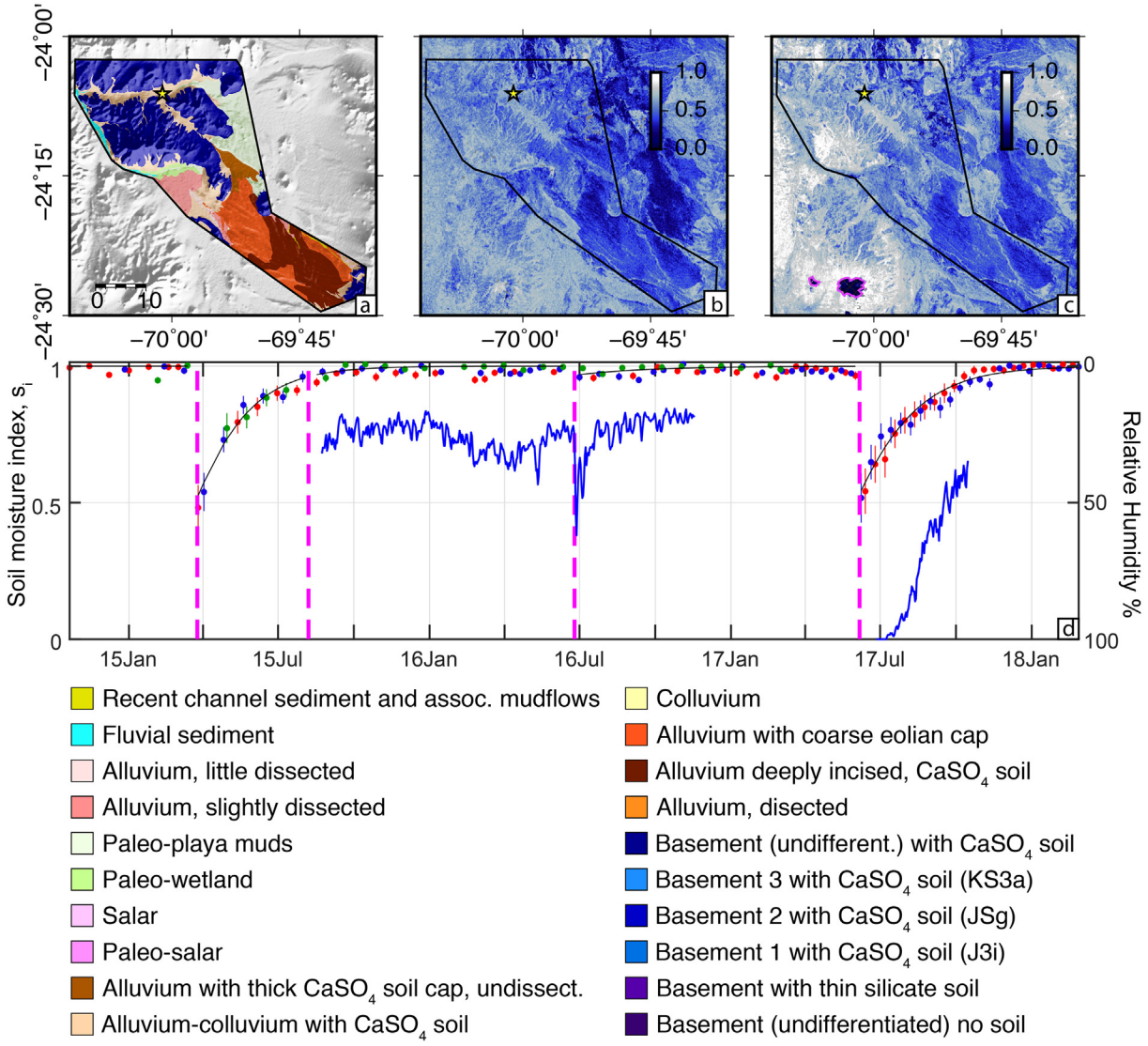

Fig. 12. Map area 1 (central polygon): a) Geological and geomorphological map. b, c) Magnitude of the best-fit exponential decay of s_i, $A_j(x)$, after March 2015 and June 2017 precipitation events, respectively. d) Time series of values of transient soil moisture at single pixel (star in a-c), with relative humidity measurement at 10 cm depth (blue curve). Other symbols as in Fig. 6. (For interpretation of the references to color in this figure legend, the reader is referred to the web version of this article.)

PW3 and PW7) are dominated by $CaSO_4$ cements, whereas the other western pits (PW4, PW5, PW6) are characterized by $CaSO_4$ horizons at depths > 30 cm. The eastern set of soil moisture pits (Fig. 3, Pits PW8 and southeastward) sample soils composed largely of silicate minerals with minor amounts of carbonate, clay, and gypsum, with the exception that sites P4 and P5 have certain horizons with high $CaSO_4$ content (Tapia, 2019).

For the nine soil pits with data from April 2015 (9–10 days after the March 2015 storm, P1–P9), the water content of the shallowest sample ranged from 1.5–7.8 wt% (Fig. 15, Table S5). P1 was sampled 9 days after the March 2015 rain event at a site where ~70 mm of precipitation fell, much of it as snow that may have melted from the sample site only 3 or 4 days prior to sampling. The other locations (P2-P9) likely received only liquid rain during March 2015. Depth profiles for the sites of repeat sampling (Fig. 15) reveal that the shallowest 15 cm in June 2015 experienced both positive (P5, P7) and negative (P4) changes of several weight % relative to two months earlier (Tapia, 2019).

There is a small InSAR coherence change associated with the March 2015 event at the P1–9 sites (Fig. S6), with a much larger signal seen on the western side of the mountains where there were no pits (Fig. 13h, i). There is some indication of rain on 21–26 May that could be responsible for the elevated moisture levels seen in pits from June 2015 (Fig. S6; sites P1, P5); the potential that it rained is corroborated by snow cover on the mountains located 20 km away (Table S4). InSAR coherence changes in the May 20–June 13 time period do indicate a large loss of coherence at high elevation to the east of these sites, presumably related to snowfall. Over the three year record at the P1–9 sites, the InSAR coherence data either do not indicate large changes for the known rain events, exhibit significant permanent coherence loss that makes it difficult to observe the transient change, or are associated with snowfall (Fig. S6).

In July 2015, for the 8 northwestern sites (PW1–8) the mean soil moisture content of the upper 10 to 15 cm was 1.5%. At the one pit (PW1) in a calcium sulfate soil with horizons and structure akin to the mature calcium sulfate soil of Ewing et al. (2006), the 23 July 2015 water content was < 0.5 wt% at all depths shallower than 60 cm, markedly drier than all other sites. There are large transient InSAR coherence signals at each of these sites (Fig. S7), but without multiple observation dates at these soil pits, we are unable to constrain the changes in soil moisture over time.

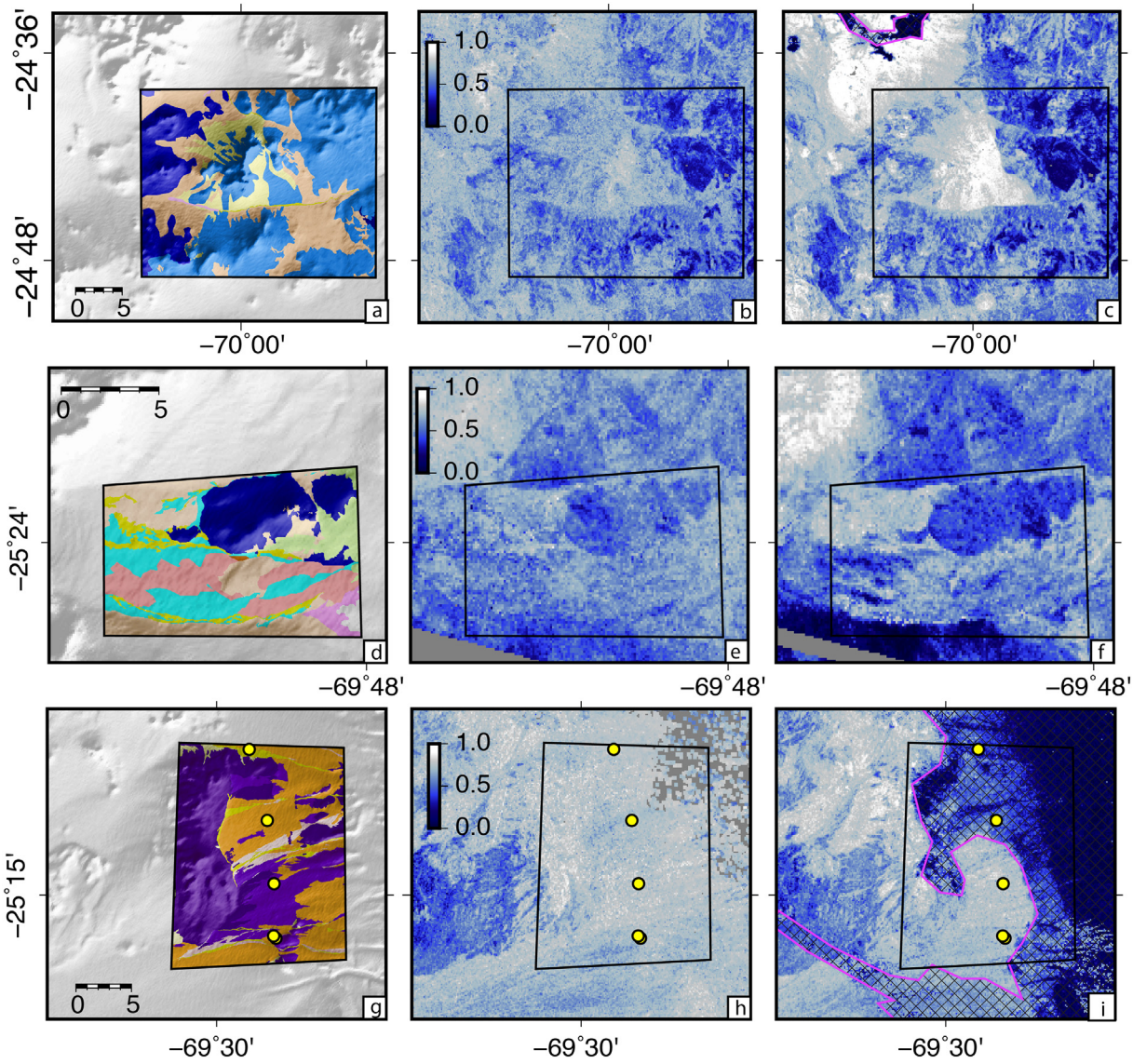

Fig. 13. Details for areas (black polygons) 2 (a–c), 3 (d–e) and 4 (f–g), and their surroundings: Left column) Geological and geomorphological mapping, legend as in Fig. 12. (middle and right columns) Magnitude of the best-fit exponential decay of s_i, $A_j(x)$, after March 2015 and June 2017 precipitation events, respectively.

The Yungay soil profile humidity data (Fig. 16) record more than a full annual cycle of seasonal variation as well as the signal associated with multiple rain events. The record began five months after the small, 7–11 August 2015 event. Rain station observations at a mine 60 km to the southeast (8.1 mm) and an airport 80 km to the NW (11.4 mm) suggest that a few millimeters of rain may have fallen at Yungay during that August 2015 event. The InSAR-based soil metric suggests that the effects of the March 2015 event may have still been lingering at the site, and does not show a significant change at the time of the 7–11 August 2015 event (Fig. 12d). The humidity data at 10 cm depth displays large variations that correlate with season (Fig. 16), with jumps at smaller rain or fog events in June 2016. Humidity observations at greater depths smoothly decrease with time since the March 2015 event, with a small perturbation in June 2016 and small magnitude seasonality. All data show a large jump after the June 2017 event, once the sensors were restarted on 25 June 2017.

6. Discussion

Previous work on the March 2015 precipitation event in the Atacama Desert (Scott et al., 2017) hypothesized that spatial variability in the time-dependent variations observed in InSAR coherence was soil type-dependent, with strong variations between regions dominated by $CaSO_4$-rich soils and silicate-mineral soils. The longer time series examined here suggests that the $CaSO_4$-rich soils and the silicate-mineral soils differ strongly in characteristics of runoff, initial infiltration of rainwater, evaporation from shallow depths, and interaction of the soil water with the mineral solids, all of which result in very different InSAR coherence behavior in response to precipitation.

6.1. Correspondence of coherence findings to landforms and surface materials

During the two rare, extreme rain events examined here, 30–90 mm of rain fell over much of the study region. The coherence for the shortest time-scale interferograms bracketing the events is very low, on order of 0.25 for many areas, which is close to the level expected for complete decorrelation. However, our use of the full set of possible interferometric pairs allows us to show that this drop in coherence was not due to permanent change of the landscape in most areas, but was due to a temporary change in soil moisture. We find that, outside of four categories of land surface (steep slopes, playas that experienced

Table 1
Summary of InSAR response in four sub-areas. Geological parent materials from Marinovic et al., 1995, and SERNAGEOMIN, 2003.

Map area	Landforms (dominant slopes)	Parent material	Soil	Transient response
1 (Fig. 12a–c)	North: mountains (5– > 10°); South: alluvial fans, pediments (< 4°)	Mesozoic granodiorite, monzogranite and tonalite; Alluvium; Colluvium	Calcium sulfate	General: very strong, long-lived response on soils. Stronger coherence loss on alluvial landforms than on mountain tops. Timescale varies in north between 2015 and 2017 events, potentially because of lower amounts of precipitation (pattern lines up with prevailing wind directions).
2 (Fig. 13a–c)	Isolated mountains (> 4°) and rolling lowlands (2–4°); Central: high peak (> 10°)	Mesozoic granodiorite and monzogranite; Mesozoic mafic to felsic volcanic rock; Colluvium; Alluvium	Calcium sulfate	Minimal response on high peak and surrounding colluvium; Strong response in hilly lowlands with extensive soil cover.
3 (Fig. 13d–e)	Northeast: mountains (3–10°); South and northwest: river valley	Northeast: Colluvium over Mesozoic diorite and monzodiorite, and bimodal volcanic rocks; Southern: deposits of streams and paleo-wetlands	Mountains: Calcium sulfate; River valley lacks soil	Strong response outside river valley. Variable to indeterminate within valley because of strong permanent coherence loss.
4 (Fig. 13g-i)	West: mountains (4– > 10°); Central and east: pediments and alluvial fans (1–5°)	Eocene granodiorite, tonalite, and diorite; Paleogene volcanic rock; Alluvial sediment	Immature silicate-mineral; minor amounts of clay, carbonate, and gypsum	Very little response in nearly all of mapped region; Small western zone with strong response corresponds to calcium sulfate soil.

flooding, anthropogenically disturbed sites, alluvial channels), most soil-mantled low slope surfaces suffered very little permanent change, irrespective of the soil composition.

As would have been anticipated by a geomorphologist, permanent changes to the surface at the scales of the InSAR coherence observations (~100 m pixels) are directly associated with landform position. On steeply sloping hillslopes in both the easternmost Domeyko Range, with silicate-mineral soils (March 2015), and locally in the Coastal Cordillera where $CaSO_4$-rich soils dominate (March 2015 and June 2017), gullying and associated debris flows observed in the field (Fig. 10) are associated with areas with permanent loss of SAR coherence (Fig. 7). In response to the extreme March 2015 precipitation event, many of the minor stream valleys that drain the eastern mountains display throughgoing permanent loss of coherence of variable degrees. Along incised channels within the Chaco River valley, the permanent coherence loss (Fig. 11e) extends all the way to the Pacific shoreline, consistent with the fact that surface flow was maintained all the way to the coastal city of Taltal, which suffered severe damage from flooding during and after the storm.

Soil type and the associated variations in water storage appear to be the major control on the strength of the transient InSAR coherence signal in the months following not only the major rain events but also the minor ones. The $CaSO_4$-rich soils are associated with large transient responses that last for months, while soils dominated by silicate minerals have a much smaller and shorter timescale response (Figs. 8, 9). The calcium sulfate soils were observed in the field to often have a fluffy texture in the upper 0 to ~25 cm, with estimated porosities of approximately 50 to 90% (Ewing et al., 2006; Owen et al., 2013). At a calcium sulfate soil pit within the study area (PW1, Fig. 2), this high porosity extends to 20 cm depth; the subjacent 40 cm is estimated to have porosity of 20%. The silicate-mineral dominated soils are also highly porous (e.g., 20–30% in the shallowest 10–20 cm), although significantly less porous than the calcium sulfate soil. Surficial layers of both soil types should permit a high degree of rain infiltration, so the observed differences may be more closely linked to how efficiently water is transported out of the system after a precipitation event.

6.2. Soil-water interactions at calcium sulfate soil sites

There are no in situ soil moisture observations in a region with $CaSO_4$-rich soil immediately after the March 2015 precipitation event. Nevertheless, soil humidity data for the Yungay site provide insight to the soil moisture conditions after two minor precipitation events (August 2015, June 2016) and after the major precipitation event of June 2017, as well as an opportunity for comparisons with the temporal history of InSAR transient coherence changes (Fig. 12).

The 10 cm depth range at the Yungay site corresponds to the lower part of a highly porous and weakly consolidated $CaSO_4$ horizon (Fig. S4) (BYK2 horizon; (Ewing et al., 2006). The 30 cm depth corresponds to a moderately well cemented gypsum horizon (By; Ewing et al., 2006). The 50 cm depth humidity probe is located within an indurated sulfate-rich interval which spans ~40 to 70 cm depth (Pfeiffer, 2018). At 10 cm depth, observed humidity varies by 10–15% on a weekly basis, and by 2–4% on a daily basis, and includes clear signals associated with the June 2016 and June 2017 events. The lingering effects of the earlier two events (which occurred before the beginning of the timeseries) are unclear and potentially masked by seasonal signals. The InSAR data, on the other hand, do not include a clear response to the June 2016 event at this location. Relative humidity observations at 30 cm and 50 cm depth decreased throughout the initial 15 months data period, and were much higher at the start of the second data period, immediately after the June 2017 event. Comparison among the trends at the three depths suggests that the March 2015 rain that originally infiltrated to 10 cm depth within the soil no longer played a role by the beginning of relative humidity observations in August 2015. In contrast, the 30 cm and 50 cm depths continued to be influenced by the

Fig. 14. Surface properties in June 2017: Photos of surface materials and landforms (detailed descriptions in Table S2) that experienced transient InSAR coherence loss as a result of the major precipitation event of June 2017. These photos correspond to dates 9 to 18 days after the precipitation event. Locations shown in Fig. 7b. Note that (a) and (b) are in regions of sulfate soils that are soft enough to leave distinct footprints (a). Location c is an alluvial surface of very immature silicate mineral soil, although it occurs in a region where calcium-sulfate soils are widespread.

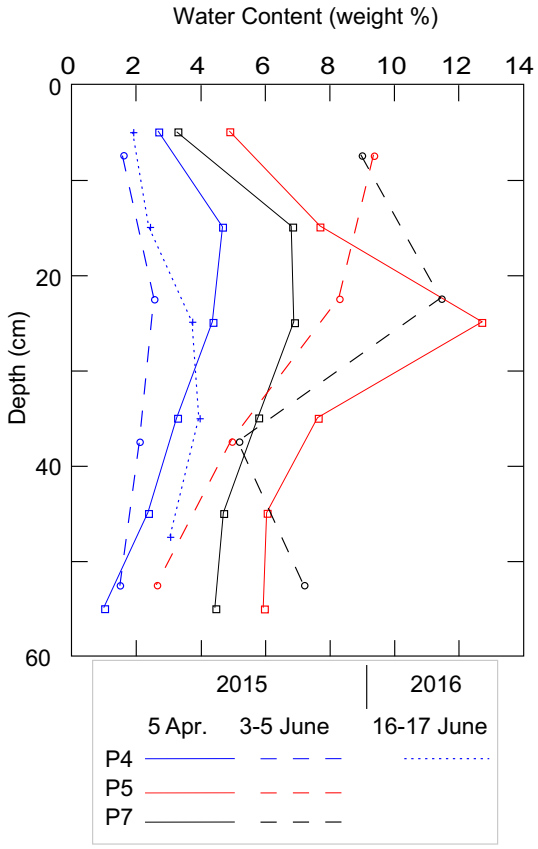

Fig. 15. Profiles: Soil moisture vs. depth for pits P4 (blue), P5 (red) and P7 (black) from the eastern, silicate-mineral based soil region (Fig. 3), for April 2015 (solid lines, about 10 days after the March 2015 precipitation event), June 2015 (long-dashed lines, winter season conditions two months later) and July 2016 (short-dashed line, 14 months later). Depths reported are mid-points of 10–15 cm thick sample intervals. (For interpretation of the references to color in this figure legend, the reader is referred to the web version of this article.)

March 2015 event until the end of 2015. The 6 June 2017 rain produced thorough wetting of the 30 cm deep horizon, with total saturation for a couple of weeks, suggesting that water pooled at the top of the indurated zone (40 cm depth). After each major event, both the 30 and 50 cm deep horizons could have continued to be sources of moisture to the shallower parts of the soil profile throughout the following months.

C-band SAR data are most sensitive to the upper few cm (e.g., Ulaby, 1981; Dobson and Ulaby, 1986) and so the coherence observations are not likely directly impacted by the soil moisture variations observed at the sensors at 30 and 50 cm depth. However, the deeper horizons may act as a reservoir that feeds moisture to the shallow horizon through evaporation, followed by condensation at shallow depths due to nighttime low temperatures. The first-order comparison between the 10 cm depth soil moisture timeseries and the InSAR transient coherence timeseries support Scott et al.'s (2017) inference that InSAR transient coherence in this region serves as a reliable proxy for relative soil moisture changes.

The mineralogy of the sulfate phase, where it has been determined, is frequently gypsum and anhydrite for locations in the hyperarid core of the Atacama Desert (Ericksen, 1981; Rech et al., 2003; Cosentino et al., 2015). At Yungay, the top 10 cm of soil contains 0.4–40% weight percent sulfate, accompanied by 0.01–0.03 wt% chloride (Amundson et al., 2012a) (Fig. S4). Sprinkling experiments near the Yungay site by Owen et al. (2013) demonstrated the high infiltration capacity of these sulfate-rich soils, at rates of 42 to 426 mm/h, even when subjected to precipitation rates much higher than likely occurred during March 2015. During those wetting experiments, the soil was uniformly wet to a depth of 3–4 cm below the surface, and irregularly wet to greater depths. Laboratory experiments have demonstrated that submersion of crushed calcium sulfate-rich soil in deionized water at room temperature leads to partial dissolution, even for short times of exposure (Bao et al., 2004). Other studies have shown that downward infiltration of rainwater over long time spans resulted in large scale, downward movement of both highly soluble NaCl and much less soluble calcium sulfate (Ewing et al., 2008; Amundson et al., 2012a).

Based on this suite of experiments and analyses, it is likely that the March 2015 rain was accompanied by some dissolution of material within the soils, infiltration of ions from the near-surface to several centimeters below the surface, and crystallization of new minerals over months as water evaporated. Given the soil profiles documented at these sites, the newly formed minerals are likely to be dominated by calcium sulfate and sodium chloride and likely form soil horizons that are slightly denser than the powdery surface material (Ewing et al., 2006; Cosentino et al., 2015; Amundson et al., 2012a). The transformation of mineral dust and surficial salts to indurated soils requires tens of thousands to millions of years (Ewing et al., 2006; Wang et al., 2015) to produce soils like those at Yungay, which implies that mass transfer in a single precipitation event by dissolution, downward transfer of ions, and precipitation of new minerals must be a miniscule fraction of the long-term total transfer of mass.

At the Yungay site, surfaces that had previously been observed in the field to have a powdery texture in the near-surface materials, became crunchy after the March 2015 rain (Pfeiffer et al., 2017). At one location, a mineralogical study after the March 2015 rain showed that the surficial layer that had previously contained anhydrite now contained only gypsum (Pfeiffer et al., 2017). Over time, the water contained in gypsum ($CaSO_4{\cdot}2H_2O$) is driven off under surface conditions

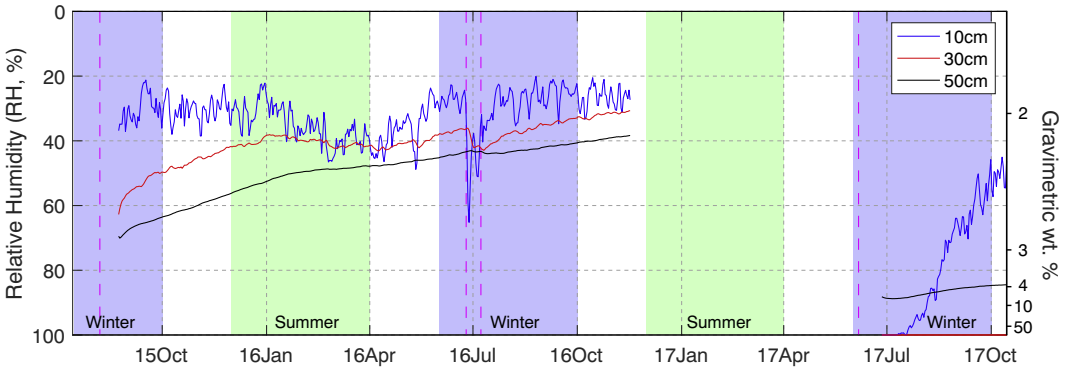

Fig. 16. Soil humidity data at Yungay: Time series of soil humidity logged at Yungay site (Fig. 2) at depths of 10 cm, 30 cm, and 50 cm, observations at 14:00 GMT (10 cm observations also shown in Fig. 12). Data span 26 months (23 August 2015–15 October 2017), with a lengthy recording gap (18 November 2016–24 June 2017). The dates of rain indicated with magenta dashed lines are documented at a rain gauge 60 km to SE (station EP, Table S4). (For interpretation of the references to color in this figure legend, the reader is referred to the web version of this article.)

in some deserts, with the resulting anhydrite rehydrating when exposed to high humidity air or other moisture sources (e.g., Herrero et al., 2009; Herrero and Porta, 2000). The surface minerals at Yungay and nearby areas had not transformed back to anhydrite before heavy rain returned in June 2017 (Pfeiffer et al., 2017).

Most sites sampled in late July 2015 (PW1–7) are in locations where calcium-sulfate soil developed on alluvial fans, and showed a strong transient coherence response (Fig. S7). However, by the time of sampling, the inferred transient coherence (heavy black lines in Fig. S7) had returned to near-normal values > 0.9 at sites (PW1–7), which is consistent with the low soil moisture values (ranging from 0.25–2.5 wt%, Table S5) observed at those sites.

Based on these observations and soil properties, we suggest that three categories of physical and mineralogical properties likely changed throughout the area of calcium-sulfate dominated soil as a result of the March 2015 rain: (i) sulfate mineral hydration state; (ii) the amount of free water in pore spaces; (iii) the vertical distribution in the soil profile of calcium sulfate, halite and more soluble salts. Given these changes, it is perhaps surprising that there is so little permanent coherence loss associated with this or later rain events across similar soils throughout the study area (Fig. 7). The lack of permanent coherence change in the InSAR observations suggests that the redistribution of solid mass per rain event is of very small magnitude. The field evidence of a change in sulfate mineral hydration state, strong transient coherence changes and subsequent return to the pre-rain state indicate that the InSAR is insensitive to the hydration state of calcium sulfate. The sulfate minerals within the soil may provide a significant source of moisture that “wets” the soil framework minerals during the months following the rain event, resulting in a longer transient coherence signal than we observe at sites where the soils do not have a significant sulfate component.

6.3. Soil-water interactions at silicate-mineral soil sites

Soil moisture measurements for nine soil pit sites within the eastern area of silicate-mineral, immature soils developed on relict alluvial fans (Table S5) provide our only in situ observation of soil moisture immediately after the March 2015 rain event, within a region that received approximately 30–50 mm of rain. InSAR coherence data are much noisier at these sites, with little to no transient coherence loss signal (Fig. S6, Fig. S7). During the April 2015 survey, two sites at high elevations (> 3400 masl, P1-P2) had high water content (7.4–7.8%) in the shallowest interval. Yet those sites have coherence timeseries (Fig. S6) that differ markedly from one another, most likely because of snow cover at P1 but not at P2. Meanwhile, the seven sites (P3-P9) in a narrow elevation range (2777–2942 masl) had a much lower mean water content (2.8% ± 1.1%) in shallow soil layers by 10 days after the event. For these, the InSAR timeseries are consistent with a slight soil moisture change on the first SAR image after the event, but no resolvable impact on soil moisture after that point. The next dates with in situ soil moisture samples for the original set of pits, in early June 2015, were two weeks after another probable rain event (Table S4), making the increased soil moisture at two of the pit sites (P5, P7) difficult to relate to progressive changes after the March 2015 event.

Field observations adjacent to soil pits P1–P9 suggest that, during the March 2015 event, infiltration dominated over runoff, such that most of the rain was at least temporarily stored in the soil (Tapia et al., 2015; Tapia, 2018). The depth profiles of soil moisture (Fig. 15) reveal that infiltration had already transferred much of the precipitation to 15–25 cm depth within the first 10 days. For one of the April 2015 soil moisture profiles (P4), paired depth profiles of pore water ^{18}O and ^{2}H suggest that the water in the upper 20 cm was freshly infiltrated from the March 24–26 rain, whereas at depths below 20 cm the April 2015 soil moisture was a mixture of pre-March 2015 remnant moisture and newly fallen rainwater (L. V. Godfrey, unpublished data). Consequently, like at Yungay, the deep soil horizons could have stored water and supplied moisture to the shallow, InSAR-sensitive zone during subsequent months. Nevertheless, the short duration of the return to full coherence (1–2 months) implies that the evaporation-condensation steps behaved differently than in the calcium-sulfate soils, or had less impact on the SAR signal. That difference may be related to the differences in porosity (typically 30% for the silicate mineral soils compared to over 50% for the sulfate soils), or to differences between the sizes of pores in the two soil classes, which were not characterized for this study. Alternatively, the distinctive InSAR transient behaviors may reflect other differences between the interactions of water with the mineral surfaces of silicates compared to sulfate minerals.

Soil pit PW8 differs from the other silicate-mineral soil locations in that it is associated with a lengthy transient InSAR response. Its soil moisture data, for late July 2015, match a still-transitional InSAR s_i value (0.82, Fig. S7) with one of the highest soil moisture observations for that date, 2.4 wt% (Table S5). Soil at PW8, located near the mapped boundary between silicate mineral-dominated and calcium sulfate-dominated soils, may represent a transitional class of materials whose soil moisture behavior and InSAR response are mixed.

The tendency through the latter part of 2015 through 2017 for precipitation to fall as snow in the region of soil pits P1–P9 (Fig. 8) may have contributed to the noisier, less well-characterized InSAR coherence behavior at the silicate soil sites. Any analysis of the relations between soil moisture changes and InSAR coherence in these relict alluvial surfaces is also made more difficult by the fact that we lack documentation of annual cycles of soil moisture variations, as all of the subsequent soil samples represent winter-season conditions (June 2015, July 2016). However, coherence changes do correlate with the timing of precipitation at these sites (Fig. S6) and there are stronger, more

long-lived transient coherence changes on fans in the area that did not happen to be sampled at the time (Fig. 13h, i).

7. Conclusions

In the past few years, a highly unusual pair of precipitation events impacted northern Chile's Atacama Desert, a normally hyperarid region with almost no vegetation. Those events, and the availability of both a detailed set of SAR data and in situ soil moisture observations, have resulted in a 3-year duration natural experiment advancing our understanding of the response of a wide range of soil types to precipitation in hyperarid regions, as well as the potential of SAR to constrain such behaviors. Here, the generally high InSAR coherence and dense time series allows us to distinguish between areas where material was actually transported in or out of the system versus areas where coherence changes were due to soil moisture variability. The spatial variations in the magnitude of the transient coherence response ($A_j(x)$, Eq. (5)) are very similar from event to event in areas where rain fell, indicating that they are dominated by variations in soil type and water storage. The characteristic timescale, $T_j^c(x)$, in areas where there was a response suggests that the water storage from these events can persist for months and replenish soil moisture within the shallowest few centimeters (the range of C-band sensitivity). Events that result in very little rain at a particularly location result in a transient coherence response with similar magnitude, $A_j(x)$, as a larger rain event, but with a much shorter timescale (Fig. 9).

The distribution of areas that had a large transient response correlates highly with regions where ground-based observations document the presence of calcium sulfate-rich soils. Silicate mineral-based soils also appear to have temporarily stored significant rain water, based on soil pit observations, but are associated with a smaller, and shorter timescale transient InSAR coherence response. The greater strength and longer timescale of the transient coherence loss in areas with calcium sulfate-rich soils relative to areas with silicate-mineral based soils suggest that the porosity or mineralogy of the calcium sulfate-rich soils allows them to retain a higher fraction of the rain water, and to renew the moisture content of their very shallowest horizons from deeper soil layers. The lack of permanent coherence loss in the fans dominated by calcium sulfate-rich soils suggests that there is little change during a single event to the solids comprising these soils, despite the dissolution, transport and recrystallization of sulfate minerals and salts that field observations suggest occurred during the precipitation events.

Strong lateral variations in the transient coherence signal that persist in character between rain events, particularly within the regions with calcium sulfate-rich soils, suggest that InSAR coherence analysis could potentially contain clues about other processes that impact soil properties. This capability may be useful for a variety of purposes, including determination of the relative ages of alluvial deposits (based on the relative maturity of the calcium sulfate deposits) for the sake of establishing histories of fault activity (e.g., Peltzer et al., 1989), or to identify areas more likely to contain enrichments of certain valuable evaporite minerals or environmental contaminants. For these purposes, additional research is needed on the interaction of SAR with calcium sulfate-dominated soils, and the effects of evaporite mineral composition and texture changes that progressively change as a result of wetting, evaporation, dissolution, and recrystallization.

While the coherence analysis performed here is greatly facilitated by the lack of vegetation and dense time series, similar soil moisture effects are certainly present within InSAR time series covering less arid regions as well. The use of coherence changes as a method for identifying locations of disturbance from processes such as earthquake-induced building collapse, landslides, or tornadoes (e.g., Schepanski et al., 2012; Yun et al., 2015; Tong and Schmidt, 2016) is likely impacted to some degree by soil moisture changes in cases where the disturbance events are also associated with storms. The magnitude of this effect can be assessed through the examination of all combinations of interferograms using the same approached shown here. Ongoing improvement to the temporal sampling and availability of SAR datasets (European Space Agency, 2013; Rosen et al., 2017) is likely to expand the range of land cover categories where these types of analyses can be performed, and allow for more quantitative analysis of the magnitude of soil moisture changes in locations where more in situ data is available.

Declaration of competing interest

The authors declare that they have no known competing financial interests or personal relationships that could have appeared to influence the work reported in this paper.

Acknowledgements

Chile's CONICYT (Comisión Nacional de Investigación Científica y Tecnológica, Chile) provided partial support through Proyecto Anillo ACT1203 (Exploration and Assessment of New Groundwater Resources in the Central Depression of Antofagasta Region). We thank Christian Herrera, Gabriel González, Javier Urrutia, Caroline Gamboa, Héctor Ramos, and Karen Centella of the Universidad Católica del Norte for field collaboration and constructive suggestions. Generic Mapping Tools (GMT) was used in generation of figures (Wessel et al., 2013). We used precipitation observations from the Dirección General de Aguas data service, available at http://snia.dga.cl/BNAConsultas/reportes. Copernicus Sentinel data from 2014 to 2018 was used in this study, retrieved from the Alaska Satellite Facility (ASF) Distributed Active Archive Center (DAAC), processed to SLC stage by the European Space Agency (ESA). R. B. L. was partially supported by NASA grant NNX16AK57G. We thank two anonymous reviewers who provided constructive criticism and suggestions.

Appendix A. Supplementary data

Supplementary data to this article can be found online at https://doi.org/10.1016/j.rse.2019.111544.

References

Amundson, R., Barnes, J.D., Ewing, S., Heimsath, A., Chong, G., 2012a. The stable isotope composition of halite and sulfate of hyperarid soils and its relation to aqueous transport. Geochim. Cosmochim. Acta 99, 271–286. https://doi.org/10.1016/j.gca.2012.04.044.

Amundson, R., Dietrich, W., Bellugi, D., Ewing, S., Nishiizumi, K., Chong, G., Owen, J., Finkel, R., Heimsath, A., Stewart, B., Caffee, M., 2012b. Geomorphologic evidence for the late Pliocene onset of hyperaridity in the Atacama Desert. GSA Bull. 124, 1048–1070. https://doi.org/10.1130/B30445.1.

Anderson, W.B., Zaitchik, B.F., Hain, C.R., Anderson, M.C., Yilmaz, M.T., Mecikalski, J., Schultz, L., 2012. Towards an integrated soil moisture drought monitor for East Africa. Hydrol. Earth Syst. Sci. 16, 2893–2913.

Baade, J., Schmullius, C., 2010. High-resolution mapping of fluvial landform change in arid environments using TerraSAR-X images. In: 2010 IEEE International Geoscience and Remote Sensing Symposium. IEEE, pp. 2159–2162.

Bao, H., Jenkins, K.A., Khachaturyan, M., Díaz, G.C., 2004. Different sulfate sources and their post-depositional migration in Atacama soils. Earth Planet. Sci. Lett. 224, 577–587. https://doi.org/10.1016/j.epsl.2004.05.006.

Born, M., Wolf, E., 1975. Principles of Optics: Electromagnetic Theory of Propagation, Interference and Diffraction of Light, 5th ed. Pergamon, Elmsford, NY.

Chen, F., Dudhia, J., 2001. Coupling an advanced land surface–hydrology model with the Penn State–NCAR MM5 modeling system. Part I: model implementation and sensitivity. Mon. Weather Rev. 129, 569–585. https://doi.org/10.1175/1520-0493(2001)129<0569:CAALSH>2.0.CO;2.

Cosentino, N.J., Jordan, T.E., Derry, L.A., Morgan, J.P., 2015. 87Sr/86Sr in recent accumulations of calcium sulfate on landscapes of hyperarid settings: a bimodal altitudinal dependence for northern Chile (19.5°S–21.5°S). Geochem. Geophys. Geosystems 16, 4311–4328. https://doi.org/10.1002/2015GC005954.

Davis, W.L., de Pater, I., McKay, C.P., 2010. Rain infiltration and crust formation in the extreme arid zone of the Atacama Desert, Chile. Planet. Space Sci. 58, 616–622. https://doi.org/10.1016/j.pss.2009.08.011. Exploring other worlds by exploring our own: The role of terrestrial analogue studies in planetary exploration.

De Zan, F., Parizzi, A., Prats-Iraola, P., López-Dekker, P., 2014. A SAR interferometric model for soil moisture. IEEE Trans. Geosci. Remote Sens. 52, 418–425. https://doi.

org/10.1109/TGRS.2013.2241069.
Delworth, T., Manaba, S., 1993. Climate variability and land-surface processes. Adv. Water Resour., Research Perspectives in Hydrology 16, 3–20. https://doi.org/10.1016/0309-1708(93)90026-C.
Díaz, C., Wright, C., 1965. Soils of the Arid Zones of Chile. Food and Agriculture Organization of the United Nations.
Dobriyal, P., Qureshi, A., Badola, R., Hussain, S.A., 2012. A review of the methods available for estimating soil moisture and its implications for water resource management. J. Hydrol. 458–459, 110–117. https://doi.org/10.1016/j.jhydrol.2012.06.021.
Dobson, M., Ulaby, F., 1986. Active microwave soil moisture research. IEEE Trans. Geosci. Remote Sens. GE-24, 23–36. https://doi.org/10.1109/TGRS.1986.289585.
Ericksen, G.E., 1981. Geology and Origin of the Chilean Nitrate Deposits (USGS Numbered Series No. 1188), Professional Paper. U.S. G.P.O.: for sale by the Supt. of Docs., GPO.
Espinoza, F.G., Matthews, S.J., Cornejo, P.P., Venegas, C.B., 2011. Carta Catalina Región de Antofagasta. (Escala 1:100,000. Serie Geología Básica 129).
European Space Agency, 2013. Sentinel-1 User Handbook.
Ewing, S.A., Sutter, B., Owen, J., Nishiizumi, K., Sharp, W., Cliff, S.S., Perry, K., Dietrich, W., McKay, C.P., Amundson, R., 2006. A threshold in soil formation at Earth's arid–hyperarid transition. Geochim. Cosmochim. Acta 70, 5293–5322. https://doi.org/10.1016/j.gca.2006.08.020.
Ewing, S.A., Yang, W., DePaolo, D.J., Michalski, G., Kendall, C., Stewart, B.W., Thiemens, M., Amundson, R., 2008. Non-biological fractionation of stable Ca isotopes in soils of the Atacama Desert, Chile. Geochim. Cosmochim. Acta 72, 1096–1110. https://doi.org/10.1016/j.gca.2007.10.029.
Farr, T.G., Rosen, P.A., Caro, E., Crippen, R., Duren, R., Hensley, S., Kobrick, M., Paller, M., Rodriguez, E., Roth, L., Seal, D., Shaffer, S., Shimada, J., Umland, J., Werner, M., Oskin, M., Burbank, D., Alsdorf, D., 2007. The shuttle radar topography mission. Rev. Geophys. 45. https://doi.org/10.1029/2005RG000183.
Fattahi, H., Agram, P., Simons, M., 2017. A network-based enhanced spectral diversity approach for TOPS time-series analysis. IEEE Trans. Geosci. Remote Sens. 55, 777–786.
Freyer, D., Voigt, W., 2003. Crystallization and phase stability of $CaSO_4$ and $CaSO_4$ – based salts. Monatshefte Für Chem. Chem. Mon. 134, 693–719. https://doi.org/10.1007/s00706-003-0590-3.
Garratt, J.R., 1994. Review: the atmospheric boundary layer. Earth-Sci. Rev. 37, 89–134. https://doi.org/10.1016/0012-8252(94)90026-4.
Hanssen, R.F., 2001. Radar Interferometry: Data Interpretation and Error Analysis. Springer.
Hao, Z., Singh, V.P., Xia, Y., 2018. Seasonal drought prediction: advances, challenges, and future prospects. Rev. Geophys. 56, 108–141. https://doi.org/10.1002/2016RG000549.
Hardie, L.A., 1967. The gypsum—anhydrite equilibrium at one atmosphere pressure. Am. Mineral. 52, 171–200.
Herrera, C., Custodio, E., 2014. Origin of waters from small springs located at the northern coast of Chile, in the vicinity of Antofagasta. Andean Geol. 41, 314–341. https://doi.org/10.5027/andgeoV41n2-a03.
Herrero, J., Porta, J., 2000. The terminology and the concepts of gypsum-rich soils. Geoderma 96, 47–61. https://doi.org/10.1016/S0016-7061(00)00003-3.
Herrero, J., Artieda, O., Hudnall, W.H., 2009. Gypsum, a tricky material. Soil Sci. Soc. Am. J. 73, 1757–1763. https://doi.org/10.2136/sssaj2008.0224.
Hossain, A.K.M.A., Easson, G., 2016. Soil moisture estimation in South-Eastern New Mexico using high resolution synthetic aperture radar (SAR) data. Geosciences 6 (1). https://doi.org/10.3390/geosciences6010001.
James, A.N., 1992. Soluble Materials in Civil Engineering. Ellis Horwood Limited.
Jordan, T.E., Riquelme, R., Gonzalez, G., Herrera, C., Godfrey, L., Colucci, S., Leon, J.G., Gamboa, C., Urrutia, J., Tapia, L., Centella, K., Ramos, H., 2015. Hydrological and geomorphological consequences of the extreme precipitation event of 24–26 March 2015, Chile. In: XIV Congreso Geologico Chileno (La Serena).
Jordan, T.E., L, C.H., Godfrey, L.V., Colucci, S.J., P, C.G., M, J.U., L, G.G., Paul, J.F., 2018. Isotopic characteristics and paleoclimate implications of the extreme rain event of March 2015 in Northern Chile. Andean Geol. 46. https://doi.org/10.5027/andgeoV46n1-3087.
Jung, M., Reichstein, M., Ciais, P., Seneviratne, S.I., Sheffield, J., Goulden, M.L., Bonan, G., Cescatti, A., Chen, J., Jeu, R. de, Dolman, A.J., Eugster, W., Gerten, D., Gianelle, D., Gobron, N., Heinke, J., Kimball, J., Law, B.E., Montagnani, L., Mu, Q., Mueller, B., Oleson, K., Papale, D., Richardson, A.D., Roupsard, O., Running, S., Tomelleri, E., Viovy, N., Weber, U., Williams, C., Wood, E., Zaehle, S., Zhang, K., 2010. Recent decline in the global land evapotranspiration trend due to limited moisture supply. Nature 467, 951–954. https://doi.org/10.1038/nature09396.
Klimchouk, A., 1996. The dissolution and conversion of gypsum and anhydrite. Int. J. Speleol. 25. https://doi.org/10.5038/1827-806X.25.3.2.
Koster, R.D., Dirmeyer, P.A., Guo, Z., Bonan, G., Chan, E., Cox, P., Gordon, C.T., Kanae, S., Kowalczyk, E., Lawrence, D., Liu, P., Lu, C.-H., Malyshev, S., McAvaney, B., Mitchell, K., Mocko, D., Oki, T., Oleson, K., Pitman, A., Sud, Y.C., Taylor, C.M., Verseghy, D., Vasic, R., Xue, Y., Yamada, T., 2004. Regions of strong coupling between soil moisture and precipitation. Science 305, 1138–1140. https://doi.org/10.1126/science.1100217.
Lee, H., Liu, J.G., 2001. Analysis of topographic decorrelation in SAR interferometry using ratio coherence imagery. IEEE Trans. Geosci. Remote Sens. 39, 223–232. https://doi.org/10.1109/36.905230.
Marinovic, S., Smoje, T., Maksaev, J., Hervé, A., Mpodozis, M., 1995. Hoja aguas blancas. Región de Antofagasta. Carta Geológica Chile 70, 150.
Mercado, G.J., 2006. Caliche, pampa y puerto: Sociabilidad popular, identidad salitrera y movimiento social mancomunal en Antofagasta, 1900–1908. Universidad de Chile.
Michalski, G., Böhlke, J.K., Thiemens, M., 2004. Long term atmospheric deposition as the source of nitrate and other salts in the Atacama Desert, Chile: new evidence from mass-independent oxygen isotopic compositions. Geochim. Cosmochim. Acta 68, 4023–4038. https://doi.org/10.1016/j.gca.2004.04.009.
Mintz, Y., 1982. The Sensitivity of Numerically Simulated Climates to Land Surface Conditions. Cambridge University Press, New York.
Mladenova, I.E., Jackson, T.J., Njoku, E., Bindlish, R., Chan, S., Cosh, M.H., Holmes, T.R.H., de Jeu, R.A.M., Jones, L., Kimball, J., Paloscia, S., Santi, E., 2014. Remote monitoring of soil moisture using passive microwave-based techniques — theoretical basis and overview of selected algorithms for AMSR-E. Remote Sens. Environ. 144, 197–213. https://doi.org/10.1016/j.rse.2014.01.013.
Moran, M.S., Hymer, D.C., Qi, J., Sano, E.E., 2000. Soil moisture evaluation using multitemporal synthetic aperture radar (SAR) in semiarid rangeland. Agric. For. Meteorol. 105, 69–80. https://doi.org/10.1016/S0168-1923(00)00189-1.
Nesti, G., Tarchi, D., Rudant, J.P., 1995. Decorrelation of backscattered signal due to soil moisture changes. In: Geoscience and Remote Sensing Symposium, 1995. IGARSS '95. "Quantitative Remote Sensing for Science and Applications", International. 3. pp. 2026–2028. https://doi.org/10.1109/IGARSS.1995.524098. Presented at the Geoscience and Remote Sensing Symposium, 1995. IGARSS '95. "Quantitative Remote Sensing for Science and Applications", International.
Nolan, M., Fatland, D.R., Hinzman, L., 2003. DInSAR measurement of soil moisture. IEEE Trans. Geosci. Remote Sens. 41, 2802–2813. https://doi.org/10.1109/TGRS.2003.817211.
Owen, J.J., Amundson, R., Dietrich, W.E., Nishiizumi, K., Sutter, B., Chong, G., 2011. The sensitivity of hillslope bedrock erosion to precipitation. Earth Surf. Process. Landf. 36, 117–135.
Owen, J.J., Dietrich, W.E., Nishiizumi, K., Chong, G., Amundson, R., 2013. Zebra stripes in the Atacama Desert: fossil evidence of overland flow - ScienceDirect. Geomorphology 182, 157–172.
Peltzer, G., Tapponnier, P., Armijo, R., 1989. Magnitude of Late Quaternary left-lateral displacements along the north edge of Tibet. Science 246, 1285–1289. https://doi.org/10.1126/science.246.4935.1285.
Pfeiffer, M.J., 2018. Water Dynamics on Landscapes and Soils of the Atacama Absolute Desert. University of California, Berkeley.
Pfeiffer, M., Howard, A.D., Heimsath, A.M., Morgan, A.M., Amundson, R., 2017. Landscape response to a century scale rainfall in the Atacama Desert, Chile. In: Presented at the GSA Annual Meeting in Seattle, Washington, USA - 2017, https://doi.org/10.1130/abs/2017AM-303668.
Rabus, B., Wehn, H., Nolan, M., 2010. The importance of soil moisture and soil structure for InSAR phase and backscatter, as determined by FDTD modeling. IEEE Trans. Geosci. Remote Sens. 48, 2421–2429. https://doi.org/10.1109/TGRS.2009.2039353.
Ramos, H.K., Riquelme, R., Centellas, K., Tapia, L., Villar, S., 2015. Determinación de agentes geomorfológicos, tectónicos y climáticos que controlan la formación de los pedimentos del flanco occidental de la Sierra de Varas -entre los −24°8′S 69°24′W - 25°10'S 69°8′W, Región de Antofagasta. In: Presented at the XIV Congreso Geológico Chileno, La Serena, pp. 1–4.
Rech, J.A., Quade, J., Hart, W.S., 2003. Isotopic evidence for the source of Ca and S in soil gypsum, anhydrite and calcite in the Atacama Desert, Chile. Geochim. Cosmochim. Acta 67, 575–586. https://doi.org/10.1016/S0016-7037(02)01175-4.
Reyes, J., Downey, P., Ossa, E., Moreno, J., Cifuentes, A., Tironi, I., Tellez, J., Petit, J., Pentenero, J., Taulis, E., Soto, E., Perez, A., Concha, G., Acevedo, P., Norambuena, C., Silva, G., Aguilera, J.M., Cicarelli, I., Mecklenburg, R., 1979. Mecánica de suelos - Determinación de la humedad (No. NCh1515.Of79). Norma Chilena Oficial. El Instituto Nacional de Normalización, Santiago, Chile.
Rosen, P.A., Gurrola, E., Sacco, G.F., Zebker, H., 2012. The InSAR scientific computing environment. In: EUSAR 2012; 9th European Conference on Synthetic Aperture Radar. Presented at the EUSAR 2012; 9th European Conference on Synthetic Aperture Radar, pp. 730–733.
Rosen, P.A., Kim, Y., Kumar, R., Misra, T., Bhan, R., Sagi, V.R., 2017. Global persistent SAR sampling with the NASA-ISRO SAR (NISAR) mission. In: 2017 IEEE Radar Conference (RadarConf). IEEE, pp. 0410–0414.
Schepanski, K., Wright, T.J., Knippertz, P., 2012. Evidence for flash floods over deserts from loss of coherence in InSAR imagery. J. Geophys. Res. Atmospheres 117. https://doi.org/10.1029/2012JD017580.
Scott, C.P., Lohman, R.B., Jordan, T.E., 2017. InSAR constraints on soil moisture evolution after the March 2015 extreme precipitation event in Chile. Sci. Rep. 7, 4903. https://doi.org/10.1038/s41598-017-05123-4.
SERNAGEOMIN, 2003. Mapa Geológico de Chile: versión digital. Publicación Geológica Digital.
Sharif, H.O., Al-Zahrani, M., Hassan, A.E., 2017. Physically, fully-distributed hydrologic simulations driven by GPM satellite rainfall over an urbanizing arid catchment in Saudi Arabia. Water 9, 163. https://doi.org/10.3390/w9030163.
Stocker, T.F., Qin, D., Plattner, G.-K., Tignor, M.M., Allen, S.K., Boschung, J., Nauels, A., Xia, Y., Bex, V., Midgley, P.M., 2013. Climate Change 2013 the Physical Science Basis.
Stocker, B.D., Zscheischler, J., Keenan, T.F., Prentice, I.C., Seneviratne, S.I., Peñuelas, J., 2019. Drought impacts on terrestrial primary production underestimated by satellite monitoring. Nat. Geosci. 12, 264. https://doi.org/10.1038/s41561-019-0318-6.
Tapia, L.S., 2019. Efectos del evento de precipitación extremo de marzo - 2015, sobre las superficies geomorfológicas y el suelo, en la Sierra de Varas, II Región de Antofagasta. Universidad Católica del Norte, Antofagasta, Chile.
Thoma, D.P., Moran, M.S., Bryant, R., Rahman, M., Holifield-Collins, C.D., Skirvin, S., Sano, E.E., Slocum, K., 2006. Comparison of four models to determine surface soil moisture from C-band radar imagery in a sparsely vegetated semiarid landscape. Water Resour. Res. 42. https://doi.org/10.1029/2004WR003905.
Tong, X., Schmidt, D., 2016. Active movement of the Cascade landslide complex in

Washington from a coherence-based InSAR time series method. Remote Sens. Environ. 186, 405–415. https://doi.org/10.1016/j.rse.2016.09.008.
Ulaby, F.T.M., 1981. Microwave remote sensing: active and passive. In: Microwave Remote Sensing Fundamentals and Radiometry. Volume 1.
Ulaby, F., Bradley, G., Dobson, M., 1979. Microwave backscatter dependence on surface roughness, soil moisture, and soil texture: part II-vegetation-covered soil. IEEE Trans. Geosci. Electron. 17, 33–40. https://doi.org/10.1109/TGE.1979.294626.
Van Genuchten, M.T., 1980. A closed-form equation for predicting the hydraulic conductivity of unsaturated soils. Soil Sci. Soc. Am. J. 44, 892–898.
Wang, F., Michalski, G., Seo, J.-H., Granger, D.E., Lifton, N., Caffee, M., 2015. Beryllium-10 concentrations in the hyper-arid soils in the Atacama Desert, Chile: implications for arid soil formation rates and El Niño driven changes in Pliocene precipitation. Geochim. Cosmochim. Acta 160, 227–242. https://doi.org/10.1016/j.gca.2015.03.008.
Wessel, P., Smith, W.H.F., Scharroo, R., Luis, J., Wobbe, F., 2013. Generic mapping tools: improved version released. EOS Trans. Am. Geophys. Union 94, 409–410. https://doi.org/10.1002/2013EO450001.
Yun, S.-H., Hudnut, K., Owen, S., Webb, F., Simons, M., Sacco, P., Gurrola, E., Manipon, G., Liang, C., Fielding, E., Milillo, P., Hua, H., Coletta, A., 2015. Rapid damage mapping for the 2015 mw 7.8 Gorkha earthquake using synthetic aperture radar data from COSMO–SkyMed and ALOS-2 satellites. Seismol. Res. Lett. 86, 1549–1556. https://doi.org/10.1785/0220150152.
Zebker, H.A., Villasenor, J., 1992. Decorrelation in interferometric radar echoes. IEEE Trans. Geosci. Remote Sens. 30, 950–959. https://doi.org/10.1109/36.175330.
Zribi, M., Kotti, F., Amri, R., Wagner, W., Shabou, M., Lili-Chabaane, Z., Baghdadi, N., 2014. Soil moisture mapping in a semiarid region, based on ASAR/Wide Swath satellite data. Water Resour. Res. 50, 823–835. https://doi.org/10.1002/2012WR013405.
Zwieback, S., Hajnsek, I., Hensley, S., 2013. Observational analysis of soil moisture effects on DInSAR signals. In: 2013 IEEE International Geoscience and Remote Sensing Symposium - IGARSS. Presented at the 2013 IEEE International Geoscience and Remote Sensing Symposium - IGARSS, pp. 4046–4049. https://doi.org/10.1109/IGARSS.2013.6723721.
Zwieback, S., Hajnsek, I., Hensley, S., 2014. Modelling the impact of moisture changes in a heterogeneous soil on differential interferometry. In: 2014 IEEE Geoscience and Remote Sensing Symposium. Presented at the 2014 IEEE Geoscience and Remote Sensing Symposium, pp. 3374–3377. https://doi.org/10.1109/IGARSS.2014.6947204.
Zwieback, S., Hensley, S., Hajnsek, I., 2015. Assessment of soil moisture effects on L-band radar interferometry. Remote Sens. Environ. 164, 77–89. https://doi.org/10.1016/j.rse.2015.04.012.
Zwieback, S., Hensley, S., Hajnsek, I., 2017. Soil moisture estimation using differential radar interferometry: toward separating soil moisture and displacements. IEEE Trans. Geosci. Remote Sens. 55, 5069–5083. https://doi.org/10.1109/TGRS.2017.2702099.